4-2016

# Creating a Computational Model of Prion Disease in the Human Neocortex

Christina Alexandra Stephens
*College of William and Mary*

Creating A Computational Model of Prion Disease in the Human Neocortex

A thesis submitted in partial fulfillment of the requirement
for the degree of Bachelor of Science in Chemistry from
The College of William and Mary

by

Christina Alexandra Stephens

Accepted for Honors
(Honors)

Randolph Coleman
Dr. Randolph Coleman, Director

Shantá D. Hinton
Dr. Shantá Hinton

Lisa Landino
Dr. Lisa Landino

Margaret Saha
Dr. Margaret Saha

Williamsburg, VA
April 28, 2016

Table of Contents

Abstract …….. 1

Introduction …… 2

Part 1: Understanding Prion Infection

1.1 An Overview of Prion Infection ……..... 6

1.2 Localization, Trafficking and Sites of Prion Conversion ……..…….. 9

1.3 Irregularity in Mitochondrial Function due to Copper Ion Deficiency …….....…10

1.4 Endoplasmic Reticulum Stress and Calcium Mobilization …….…….... 18

1.5 Cytosolic and Nuclear Signaling Response to Reactive Oxygen and Nitrogen Species-Related Damage……... 18

1.6 Exogenous Stress Response Signaling ……. 24

1.7 Phagocytosis of Apoptotic Cell Material by Macrophagic Microglial Cells …… 25

Part 2. Creating an Illustrative 'Map' of Prion Infection using CellDesigner Software

2.1 Model One: Reactive Oxygen Species Generation During Prion Infection ……. 26

2.2 Model Two: Whole-body Trafficking of Prion Infection …… 27

2.3 Model Three: Trafficking of Prion Protein and Cellular Response to Damage Related to Prion Infection in the Neocortex …….……. 29

Model in Four Parts:

1. Localization and Trafficking …….…….…. 29
2. Mitochondria ……..…. 30
3. Nuclear and Cytosolic Trafficking ……..…… 32
4. Microglial Activation and Phagocytosis ……..... 34

Part 3: Coding Prion Infection as Sequential and Interdependent Kinetic Equations in Matlab

3.1 Explanation of Complex Enzyme Kinetics …… 36

3.2 Why Use Matlab? ……... 38

3.3 Assumptions Taken in Coding Process …….. 40

3.4 Applying Kinetic Equations to More Than One Cell ……..… 43

3.5 Results of Kinetic Model …… 45

Part 4: Generating A Spatial Approximation of the Human Neocortex in Matlab

4.1 Cylindrical Approximations of Neurons …… 50

4.2 Visualization of Cylindrical Approximations ……... 53

4.3 Derivation of Axonal and Dendritic Branch Densities …….. 57

4.4 Derivation of Density Probability Equation ……..…. 62

Part 5: Combing the Kinetic Equations with the Spatial Representation

5.1 Methodology ……..… 69

Discussion ……..…… 73

Conclusion ……74

Acknowledgments …… 76

Sources ……..…… 77

Appendix

Images of CellDesigner Model

a. Localization and Trafficking ……. 88

b. Mitochondria ……. 89

c. Nuclear and Cytosolic Trafficking ……... 90

d. Microglial Activation and Phagocytosis ……..….. 91

Matlab Code

Presented in a supplementary document

## Abstract

One way to study disease is to model specific biological reactions or processes involved in the generation of the disease in terms of a system of differential equations. The equations, called kinetic rate laws, are often non-linear and high order, making them difficult to solve. By approximating equations in complex biological networks as linear first order reactions, we can solve large sets of equations using computational software, such as MATLAB, to determine general trends in the change of molecular concentrations over time. These trends can tell us details about the disease and direct us toward areas worthy of further investigation. We can gain additional information concerning the potential behavior of a disease by superimposing its signaling network over a spatial approximation. In our work, we were able to generate a representation of a small volume of the human neocortex by modeling neurons cylinders. Cylinders act as a reliable model to describe the approximate radial symmetry of neurons. We also derived probability density equations for the dendrites and axons of each neuros. The model system is flexible so that any set of differential equations can be superimposed onto it. We plan to run our own devised system of equations for prion disease on the spatial model to see how its results differ from those produced by the kinetic equations alone.

# Introduction

Approximations allow us to study systems that are too complex to be observed directly. Chemists, physicists, mathematicians, and biologists make what some may call assumptions in order to generalize what they could only feasibly determine for a single case. By using approximations, scientists can predict and even model future events. For example, no one has yet to solve the Schrödinger equations exactly for any molecule beyond hydrogen, but there have been great approximations that have given us results that align very well with what is observed for larger atoms and molecules. Biologists use a set of equations that describe genetic variations in population equilibria known as the Hardy-Weinberg equations, again based on a set of reliable assumptions. Sometimes an approximation is the closest we get to the real thing. We may not know the exact result of an experiment, observation or potential event, but if we make certain assumptions, we gain results that help us understand what is actually happening or may happen. We can, as we have demonstrated in our work, apply the use of approximations to study very complicated systems. Disease, particularly when studied at a molecular level, is a great example of a complex system. Even the diseases we now know how to treat, we may still not know the exact mechanisms of or means to treat more effectively. Scientists have made significant strides by focusing on one or two components of the disease at a time, but imagine being able to investigate tens and even hundreds of components at a time. By compiling results of individual studies and modeling many significant components of the disease at once, we can draw conclusions about the whole system that would have otherwise been unrealized.

We choose to demonstrate the use of disease modeling by creating a spatial-kinetic model of prion disease, a rare kind of neurodegenerative disease affecting less than one in one million people each year. Of the reported cases, only a small percentage have been related to the familial

forms of the disease caused by gene mutation in the PRNP gene called Creutzfeldt-Jakob disease (CJD), Gerstmann-Strässler-Scheinker syndrome (GSS) and fatal familial insomnia (FFI). The remainder and majority of cases (85-90%) have been related to either sporadic CJD (sCJD), in which the protein $PrP^C$ spontaneously misfolds into a toxic isoform, or acquired prion infection called variant CJD (vCJD), when an individual internalizes prion protein after consuming contaminated material or having accidentally been exposed to contaminated material. The importance of studying this disease goes beyond care for those affected by it but also for the benefits understanding the disease mechanism would have. There is still no means of treating and effectively diagnosing prion infection, however its similarity to other aggregate-based diseases such as Alzheimer's disease and Huntington's disease allows researchers to draw conclusions on how best to treat these conditions.

Modeling a disease system using computational software is a neat way of simulating reactions and physical processes using equations, but first we need to gather the information on which the equations are based. This process is analogous to gathering all the pieces of a puzzle and arranging them so that they resemble and explain how a disease works at the molecular level. This model can then be manipulated to reflect different starting conditions and return whatever outcome a potential live cell system would produce. Modeling removes the necessity for trial and error experiments using traditional and often expensive traditional lab techniques, by determining what may be the most productive area to focus on for researchers. Much has already been accomplished in the field of enzymology, however, by taking a purely mathematical approach, which greatly simplifies the system, we believe we gained new insights in the understanding of the disease process (Edelstein-Keshet, 2005).

Over the past year we have developed such a model of prion infection in the human brain. The general methodology behind similar modeling efforts in the past has been to generate a large number of differential equations representing enzymatic kinetic reactions found to be vital during infection, and then to evaluate the reactions' change in activity and concentration. These general rate equations have provided important data in the past, however it lacks additional conditions that a real cellular environment may have such as intercellular interaction, spatial limitations, distribution of molecules, and movement of cells. The goal of our research has been not only to provide a model of the enzymatic processes effecting and driving prion toxicity, but to also evaluate those processes in a system that more accurately reflects the dynamism of live systems. In building our model we also attempted to preserve a bottom-up design mentality. Bottom-up designing involves constructing small sub-systems and then combining them to form a larger, more complex system. Essentially, starting a model in this way minimizes the risk of overdesign, meaning to model such that it reflects what is to be expected rather what the model should produce when constructed using only basic assumptions and knowledge about cellular systems. The hope is that by modeling a general system from the ground up and then applying specific conditions present in prion disease derived from published literature, we can achieve unbiased results. Additionally, we then have a general modeled system of a human brain to which any number of disease conditions can be applied, and it will output results specific to that disease.

There were three major processes in our modeling methodology. The first was to extensively research the disease and dedicate more focus on areas we found to be significant factors in in the disease process. The information was then organized into an illustrative signaling network involving molecules and macromolecules key to the disease's function by

using a software program called CellDesigner. The second process was to translate the illustrative model into a set of time-dependent differential equations, called classic kinetic equations that could be solved to compute the concentration of a given molecule over time. The equations were inter-dependent, for example say an enzyme may effect the concentration of product used in a separate enzymatic process. There are number of databases we used, including MOPED and BRENDA, to obtain cellular concentrations. The third major process was then designing a three-dimensional representation of the human neocortex, on which we could overlay the classic kinetic equations. I choose to model the disease in the neocortex for the diversity in its cellular composition. We were able to generate code that approximated the volumes occupied by the dendrites, soma, and axons of a few neuronal subtypes called pyramidal and stellate cells. This was done in a way that the probability overlap of axons and dendrites could be calculated, as well as the number of synapses formed with a given neuron. We chose to model the neurons as cylinders in order to reflect the approximate natural symmetry of a few phenotypes and were able to determine a density equation for the dendrites and axons of each neuronal phenotype. These equations were then used to generate probability densities of dendritic and axonal branches utilized in the enzymatic equations to better reflect molecular distributions.

# Part 1: Understanding Prion Infection

## 1.1 An Overview of Prion Disease

Prion disease is similar to other neurodegenerative diseases characterized by abnormal accumulation of protein aggregates, but has a unique infectious pathology. Though variations of prion disease have been strongly correlated with genetic factors; others like those focused on in this project are transmissible. Variant Creutzfeld-Jakob Disease (CJD) is a form of prion infection where the misfolded isoform of the normal glychophosphatidylinositol (GPI)- anchored protein, $PrP^{C}$, called $PrP^{Sc}$ or scrapie protein, enters and proliferates within an individual from an external source. $PrP^{Sc}$ mostly likely accumulates within the body's lymphatic system following uptake from the intestinal lumen (Michael et al., 2012). Follicular dendritic cells in germinal centers of lymphnodes and later the spleen serve as sites of replication. Integration of the circular system allows $PrP^{Sc}$ aggregates enter the blood stream and peripheral nervous system (PNS), through which they will eventually enter the central nervous system (CNS). When $PrP^{Sc}$ comes in contact with $PrP^{C}$ it is able to convert the normal isoform to the scrapie protein (Nishima et al., 2004). The mechanism by which this occurs is not currently understood. Symptoms of CJD include dysfunction of cells within the CNS, neuroamyloid formation, neuronal death, brain inflammation, generation of reactive oxygen and nitrogen species, and dementia (Soto et al. 2012). These symptoms are shared with other diseases generalized as transmissible spongiform encephalopathies (TSEs) (Bush, 2000). Prion infection may occur through interspecies transmission (a postulated explanation for the outbreak of 'mad cow disease' in the mid-1990s) (Kozlowski et al., 2009). Evidence of scrapie protein within sheep, cattle deer, and other mammals support this theory. Due to the inconsistency between misfolded isoforms there is no

current successful treatment for prion infection and though extremely rare, it remains highly contagious and fatal **(**Kozlowski et al., 2009**)** (Bush, 2000).

The CNS is a central area of interest during prion infection as $PrP^{C}$ is widely expressed in CNS glial cells and neurons, though $PrP^{Sc}$ may also infect cells within the lymphatic system and spread throughout the bloodstream and PNS as a means to bypass the blood brain barrier (BBB) and enter the CNS (Cho et al., 2013) (Jeon et al., 2013). $PrP^{Sc}$ infection is mostly localized within the neocortex (Bush, 2000). Once $PrP^{Sc}$ enters the CNS and comes into contact with $PrP^{C}$ either on the plasma membrane or within endolysosomal compartments it disrupts the normal function of the cell (Campana et al., 2005). Several theories exist on how prion infection induces cell damage and potential apoptosis. Our model synthesizes many components contributing to dysfunction. The loss of function of $PrP^{C}$ may be the initial and driving cause of oxidative stress and metal dyshomeostasis. $PrP^{C}$ can bind several divalent metal ions important to normal cellular function (Singh et al., 2012). It has different affinities for several metal ions including copper (II), zinc (II) and iron (II), of which copper has the highest affinity. Binding of Zn and Cu to $PrP^{C}$ triggers its internalization into endosomes, release of the metal ions into the cytosol, and the protein is either recycled to the plasma membrane or degraded (Campana et al., 2005). Many researchers have concluded that due to its ability to bind copper and zinc as well as its localization at synaptic clefts, $PrP^{C}$ may be an important component to cell depolarization. Additional research has found that $PrP^{C}$ serves as a natural dismutase or antioxidant function through various mechanisms possibly by metal ion regulation or use of bound, redox-active metal ions to reduce ROS and RNS (Haigh et al., 2011). The build up of oxidative stress appears to be concurrent to increased transcription of PRNP (the gene encoding $PrP^{C}$) further suggesting its cell protective role (Urso et al., 2012). The loss of $PrP^{C}$ by induced conversion to $PrP^{Sc}$ could

therefore deplete means by which the cell decreases oxidative stress. The function of antioxidant metalloproteins such as Zn, Cu-superoxide dismutase would also suffer due to the reduced metal ion uptake (Haigh et al., 2011). Molecular consequences of prion infection shared with other neurodegenerative diseases such as Alzheimer's, Parkinson's, and Amyotrophic Lateral Sclerosis include the build up of protein aggregates, oxidative damage by reactive oxygen and nitrogen species (ROS and RNS), and disruption of metal ion homeostasis (Kozlowski et al., 2009).

The generation of oxidative stress is not limited to the loss of function of $PrP^{C}$. The structure of $PrP^{Sc}$ consists of heavily packed beta-pleated sheets that form amyloid aggregates. These aggregates are trafficked in endolysosomes or autophagolysosomes for degradation. Aggregates are known to be resistant to proteinase K (PK) degradation and may accumulate within theses intracellular compartments and increase lysosomal ROS generation (Haigh et al., 2011). Accumulated ROS and RNS within the cell disrupt the integrity of lipid membranes and may cause additional oxidative species to 'leak' form lysosomal compartments into the cytosol (Öllinger et al., 1995).

The proliferation of oxidative stress and potential retrograde trafficking of $PrP^{Sc}$ could induce endoplasmic reticulum (ER) stress, increasing misfolding events and contributing to cytosolic PK-resistant $PrP^{C}$ aggregates (Campana et al., 2005). Oxidative species can also oxidize DNA within the nucleus. The build-up of oxidative stress, ER stress, and DNA damage triggers activation of both cell-survival and pro-apoptotic signaling molecules such as NF-κB and p38 MAPK. Transcription factor FOXO3a is a central proteins in the pro-apoptotic signaling cascade induced by oxidative stress. Cell signaling induces a mitochondrial apoptotic mechanism and production of intercellular signals such as TGFβ (Biber et al., 2007). The release of these a extracellular signals related to stress response induces activation of local astrocytes, microglia,

and oligodendrocytes (OLGs) which subsequently release additional signals that enact migration of other glial cells and immune cells (induction of inflammation) or influence additional cell death signaling in infected neurons (Urrutia et al., 2014). The molecular details for signaling within local astrocytes are not discussed in this paper. However, we have illustrated that both neurons and astrocytes are susceptible to prion infection in our earlier model (Lima et al., 2007). Disruption of normal astrocyte function could lead to accumulation of the neurotransmitter glutamate within the extracellular space and induce excitotoxicity within the neuron through calcium influx (Asuni et al., 2013).

Our model does not include all of the metabolic details related to prion infection, but focuses on the following areas: $PrP^{C}$ conversion to $PrP^{Sc}$, endocytosis and autophagy of $PrP^{Sc}$ aggregates, metal ion dyshomeostasis, mitochondrial dysfunction, ROS and RNS generation, ER stress, stress response signaling, and local microglia activation.

## 1.2 Localization, Trafficking and Sites of Prion Conversion

Portions of the plasma membrane called lipid rafts are saturated with cholesterol, sphingolipids, and GMI gangliosides which makes them highly mobile within the membrane. GPI-anchored $PrP^{C}$ are typically localized within lipid rafts on the cell surface and are most likely the initial sites for $PrP^{C}$ to $PrP^{Sc}$ conversion (Shi et al., 2014). Strong evidence supports that $PrP^{C}$ is normally internalized via endocytosis following metal ion ligation, further discussed below (also see figure 1). $PrP^{C}$, along with lipid raft components are then heavily recycled back to the plasma membrane (Botto et al., 2014). Beta pleated sheet rich conformations of $PrP^{C}$ like $PrP^{Sc}$ are not compatible with lipid rafts and are likely displaced (Watt et al., 2013). It is likely that displaced $PrP^{Sc}$ aggregates are endocytosed and targeted for degradation within

endoslysosomal compartments (Botto et al., 2014). Cells affected by Alzheimer's show that beclin-1 protein re-localizes to lipid membranes containing $PrP^{C}$ aggregated with amyloid beta, aiding vesicle formation for autophagy (Nah et al., 2013). Beclin-1 may similarly be sequestered into lipid rafts containing $PrP^{C}$ bound to $PrP^{Sc}$ in a similar process. The protective function of $PrP^{Sc}$ endocystosis may actually contribute to increased aggregation events by providing sites for close $PrP^{Sc}$-$PrP^{C}$ interactions. $PrP^{C}$ may be converted within intracellular compartments when co-localized with $PrP^{Sc}$ (Botto et al., 2014). Accumulation of degradation-resistant $PrP^{Sc}$ in acidic oxidizing compartments produces a lysosomal burst of ROS during early prion infection (Haigh et al., 2011).

$PrP^{Sc}$ within the cytosol can be targeted for degradation by proteasomes through the ubiquitin proteasome system (UPS). Polyubiquinated $PrP^{Sc}$ can actually interact with the 20s region of proteasomes and impair its own degradation. $PrP^{Sc}$-induced proteasomal dysfunction slows UPS response causing a build up of polubiquinated $PrP^{Sc}$ in the cytosol (Xu et al., 2005). The cell can mediate impaired UPS response through activation of nuclear factor (erythroid-derived 2)-like 2 (Nrf2), which increases expression of p62. An increase in p62 levels is typically associated with prion infected cell cultures. p62 binds polyubiquinated aggregates, like $PrP^{Sc}$, and promotes internalization into autophagosomes (Homma et al., 2014).

## 1.3 Irregularity in Mitochondrial Function due to Copper Ion Deficiency

Copper, zinc, iron and several other metals are under strict regulation within the brain in order to maintain homeostatic balance. These three metals named were focused in this project for their contributions to ROS and RNS generation in a prion-infected neuron. Only two of these metals are capable of redox chemistry: copper and iron. They directly contribute to ROS by

directly catalyzing free radical generation from hydrogen peroxide ($H_2O_2$), a byproduct of oxidative respiration (Kozlowski et al., 2009). Dependent on its intracellular concentration, Zn can have an antioxidant function via contribution to SOD, a neuroprotective function by induction of metallothionein, or become neurotoxic by assisting excititoxicity. $PrP^C$ can bind all three metals with differing degrees in affinity (see Figure 2).

$PrP^C$ has an approximately 1000 fold higher binding affinity for copper (II) than Fe and Zn (Nishina, 2004). Many studies conclude that $PrP^C$ binds copper cooperatively by its N-terminal octapeptide domain. Whether or not the octapeptide region is necessary for copper binding is debatable, as a few studies have demonstrated that truncated $PrP^C$ can also bind copper (Nishina et al., 2004). The octapeptide tetra-repeat binding domain contains histadine and methionine which may act as electron donors in the reduction of bound Cu(II). The copper held by the domain may also reduce oxygen ($O_2$) in producing $H_2O_2$ (Bush, 2000). Hydrogen peroxide may continue to react with Cu(I) held by octapeptide domain in metal-catalyzed oxidations, generating hydroxyl radicals ($HO^- \cdot$) and immediately oxidizing amino acid residues (Kozlowski et al., 2009). Oxidized methionine ($Met^{ox}$) and histidine (2-oxo-His) residues within the protein's hydrophobic region are found in a large portion of PK-resistant PrPSc. Reactions with $H_2O_2$ also decrease the stability of $PrP^C$ by 9 kJ/mol. Reactions of bound copper and $H_2O_2$ may therefor aid $PrP^{Sc}$ conversion. If a reductant is present Cu(II) held by $PrP^C$ may form oxidative species (Younan et al., 2012).

The copper-binding domain is retained in the scrapie protein, however the misfolding event may increase exposure of the bound copper to its surroundings, increasing contact with potential reductants. When bound to $PrP^C$, Cu(II) may be shielded from reductants other than the histadine and methione residues within the binding domain (Bush, 2000). In later stages of prion

infection, once ROS and RNS have accumulated with the extracellular space, redox reactions with copper bound to $PrP^{C}$ and $PrP^{Sc}$ may become more likely and contribute to the growing pool of oxidants.

Copper bound to $PrP^{Sc}$ can induce conformational change that increases the protease resistance of $PrP^{Sc}$ under low ionic strength (Nishima, 2004). Ligated Cu(II) can even accelerate protein aggregation (Kozloowski et al., 2009). The binding of not only copper, but other metal ions induce conformation changes in the properly folded and misfolded protein, allowing variant and reversible conformations to exist. Conformations that are resistant to protease, but are not capable of inducing misfolding of $PrP^{C}$ are here called $PrP^{Res}$. The degree PK resistance and stability of the misfolded conformation is sensitive to ionic strength. An experimental concentration of 50$\mu$M NaCl was necessary for this stability. The minimum ionic strength provides $PrP^{Sc}$ and $PrP^{Res}$ with sufficient shielding between electrostatically repulsive residues, contributing to their stability. $Pr^{C}$ is 1000 and 2000 fold more sensitive to PK resistance under low and high ionic concentrations than PK-resistant structures (Nishima, 2004). Experimental concentrations for maximized protease resistance range from 30 to 40$\mu$M (Nishima, 2004).

Binding of Cu(II) stimulates clathrin-mediated endocytosis under low intracellular ion concentrations (Urso et al., 2012). Once in an early endosomal compartment, Cu(II) is released from $PrP^{C}$ into the cytosol where it is most likely chaperoned to appropriate metalloproteins. $PrP^{C}$ is then either trafficked back to the plasma membrane or degraded within endolysosomes. Given the stability of ionic strength within endosomal compartments, $PrP^{Sc}$ and $PrP^{Res}$ , whether or not bound to metal ions, will not be degraded as much or as quickly as $PrP^{C}$ and continue to accumulate. Metals still bound to the misfolded conformations within the cell are degraded at a slower rate than conformations not bound to a metal. Even at low ionic strengths such as those

experienced within endosomal compartments, binding of Cu and Zn increases $PrP^{Sc}$ and $PrP^{Res}$ stability. Bound redox-active metals (copper and iron) may continue to form oxidative species within the cellular compartments.

The total amount of metal ions within the brain are not likely to fluctuate due to the relative impermeability of the blood brain barrier to plasma metal ions. Levels of copper, iron, and zinc present in the brain are within an order of magnitude that can sufficiently produce neurotoxicity during stress (Bush, 2000). Natural cellular responses to restore normal ion levels may overcompensate or become over activated due to continuous proliferation of the prion protein and subsequent ion depletion. Both early depletion and later accumulation of metal ions within infected neurons can cause the formation of ROS and RNS, which is closely associated with infection (Uttara et al., 2009).

Copper, largely present as Cu(II) outside of cells is transported into neurons by plasma membrane proteins copper transporter 1 (CTR1), DMT1, and endocytosis following $PrP^{C}$ ligation (Nelson, 1999). The first two can sustain 50% of both Cu(I) and Cu(II) transport (Urso et al., 2012). DMT1 transports Cu(II) and also mediates a significant portion of Zn(II) and Fe(II) import. CTR1 is specific for Cu(I) and transports Cu(I) out of endosomal compartments and aids its delivery to cytosolic chaperones (Kozlowski et al., 2009). Under normal cellular conditions copper does not remain free within the cytosol, but is delivered to various cuproenzymes like Cu,Zn superoxide dismutase (Cu,Zn SOD) (Prohaska et al., 2004). Free copper within the cytosol can produce ROS (Kozlowski et al., 2009). Copper acts a cofactor for a large number of proteins and participates in various non-enzymatic processes not limited to antioxidant functions, but they're not featured here (Urso et al., 2012). A large portion of copper is utilized within the mitochondrial inner membrane. $PrP^{Sc}$ aggregates with Cu(I) and localize within endolysosomes.

Due to the increased stability of $PrP^{Sc}$ bound to copper, less copper may be released into the cytosol.

Depletion of copper can lead to irregular activity of cuproenzymes including important antioxidant proteins. A build up of intracellular ROS is typically associated with metal ion imbalance and potentially due to the loss of function of Cu,ZnSOD. During events of intracellular copper depletion the cell will attempt to restore normal levels through increased relocalization of CTR1 and DMT1. $PrP^{C}$ is also upregulated during periods of copper depletion. The increase in $PrP^{C}$ expression increases the catalytic efficiency of copper transport (Urso et al., 2012). Increased expression is also capable of recovering decreased SOD function. Many sources claim that $PrP^{C}$ has a natural antioxidant function not only by mediating metal-catalyzed redox reactions, but its importance in metal ion homestasis and delivery of essential cofactors to antioxidant metalloproteins gives it an overall neuroprotective quality.

Oxidative stress within the mammalian brain is caused by a build up of ROS and RNS and strongly linked with a number of neurodegenerative diseases. The brain is particularly susceptible to oxidative damage due to high oxygen consumption for continuous production of ATP (Kovacic et al., 2012). As a consequence of high oxygen consumption, 1-2% of imported oxygen is converted to ROS during the reduction process of oxidative phosphorylation (Kozlowski et al., 2009). Another major source of ROS is fatty acid peroxidation which consumes approximately 20% of $O_2$ (Uttara et al., 2009). Lipid peroxidation products include 4-hydroxynonenal and 4-oxononeneal, which are themselves reactive species (Kovacic et al., 2012). The cell has built-in mechanisms to handle low levels of ROS including the use of localized enzymatic antioxidants catalase, glutathione peroxidase and superoxide dismutase (Uttara et al., 2009). Two forms of superoxide dismutase (SOD) occur in the cell: MnSOD found

within the mitochondria and Cu,ZnSOD typically found throughout the cell (Sinclair et al., 2013). The ubiquitous nature of Cu,ZnSOD is important as superoxide ($O_2^-$) produced in the mitochondria can freely diffuse out of the organelle and into the cytosol. Dismutation of $O_2^-$ to $H_2O_2$ is an important step preventing free radical reactions of $O_2^-$ with membrane lipids and nitrogenous molecules (Carreras et al., 2007). Products of $O_2^-$ reactions like the hydroxyl radical (·OH) can be more reactive and more readily diffusible (Uttara et al., 2009). SODs catalyze the following reaction:

$$O_2^- \cdot + O_2^- \cdot + 2H^+ \rightarrow H_2O_2 + O_2$$

$H_2O_2$ is still capable of oxidizing reductants it comes in contact with within the cytosol. Cell arrest can occur if $H_2O_2$ concentration reaches levels greater than $100\mu M$ through specific signaling stimulation. $H_2O_2$ is further reduced by antioxidant enzymes catalase and glutathione peroxidase (GPx), which are present within mitochondria and throughout the cytosol (Carreras et al., 2007). Increased ROS increases amounts of oxidized glutathione. Glutathione redox cycles are vital to $NAD^+$ redox cycles (Urrutia et al., 2014). Imbalance of glutathione states due to greater amounts of $H_2O_2$ and disruption of mitochondrial membrane integrity may reduce its ability to mediate antioxidant response. GSSG also contributes to Zn(II) release by oxidizing metallothionein (Bush, 2000). See figure 4 for mitochondrial ROS and RNS production.

a. catalase

$$H_2O_2 \rightarrow 2H_2O + O_2$$

b. GPx

$$H_2O_2 + 2GSG \rightarrow 2H_2O + GSSG$$

Increased ROS species during prion infection is likely a combination or $PrP^{Sc}$ aggregate accumulation in intracellular compartments and irregularity in metal ion uptake which can deplete antioxidant function of Cu,ZnSOD. In later stages of accumulation redox-active copper and iron catalyze more radicalization (Bush, 2000). Lysosomal compartments containing $PrP^{Sc}$ aggregates and loosely bound metal ion produce a significant amount of ROS. Though $H_2O_2$ can diffuse out of compartments, increased peroxidation of membrane lipids destabilizes lysosomal membrane structure, which could allow leakage of reactive species and aggregates into the cytosol (Öllinger et al., 1995). Iron is a key component of oxidative stress both during periods of apparent deficiency and accumulation. Unavailability of sufficient levels of iron can cause disruption of electron transport chain interactions leading to more electron leakage events and free radical formation (Urrutia et al., 2009). Excess amounts of iron is poorly bound to appropriate enzymes and produces free radicals via autocatalyic Fenton and Harber-Weiss reactions. (Kovacic et al., 2012) (Uttara et al., 2009).

a. Fenton Reactions

$$Fe^{3+} + \cdot O_2^- \rightarrow Fe^{2+} + O_2$$

$$Fe^{2+} + H_2O_2 \rightarrow Fe^{3+} + HO^- + \cdot OH$$

b. Harber-Weiss Reactions

$$\cdot O_2^- + H_2O_2 \rightarrow O_2 + OH \cdot + OH^-$$

ROS generation throughout infection may not be an exponential increase but can be characterized by four stages of oxidative response: acute, adaptive, chronic, and terminal

(Sinclair et al., 2013). ROS typically correlates with levels of $PrP^{Sc}$ aggregates and may experience a similar plateau of propagation and proliferaction without neurotoxic consequences (Jallad et al., 2014). Initial ROS production may be handled by a cellular stress response, but continuous infection eventual overwhelms the cells ability to quench ROS and RNS (Haigh et al., 2011). At a critical point of oxidative stress, the cell begins to favor expression of pro-apoptotic factors over pro-survival factors. Pro-apoptotic signaling can result in cell-induced ROS and RNS generation to accelerate apoptosis. Such signaling increases expression and activation of NADPH oxidase, inducible nitric oxide synthase (iNOS) in microglial cells and neuron nitric oxide synthase (nNOS). NADPH oxidase increases superoxide production and NOS enzymes produce nitric oxide (Haigh et al., 2011).

Nitric oxide synthase forms nitric oxide (NO) from 1-arg and $O_2$. Increased NO reacts with $O_2^-$ to form RNS peroxynitrite ($ONOO^-$). Higher levels of NO decrease oxidative phosphorylation activity by up to 50% by interrupting cytochrome c oxidase $O_2$ consumption (Carreras et al., 2007).

$$O_2^- \cdot + NO \rightarrow ONOO^-$$

NO and $H_2O_2$ can mediate further activation of pro-apoptotic signaling through MAPK activity, discussed in detail later. ROS and RNS increase lipid peroxidation events and increase permeability of organelle membranes including the mitochondria. Accumulated ROS and RNS can also oxidize DNA within the nucleus and triggers additional cell death pathways. One such pathways involves increasing the permeability of mitochondria allowing greater uptake of $Ca^{2+}$ and Zn(II) which disrupt normal function and contribute to mitochondrial oxidative stress (Kozlowski et al., 2009).

## 1.4 Endoplasmic Reticulum Stress and Calcium Mobilization

Stress to the endoplasmic reticulum (ER) is also associated with prion infection. The ER is a major storage unit for intracellular $Ca^{2+}$. Efflux of $Ca^{2+}$ from stressed ER contributes to activity related to excitoxcicity, which includes stress-response signaling and increased permeability of mitochondrial membranes. ER stress may first be induced by accumulation of $PrP^{Sc}$ aggregates within the organelle and by later oxidative stress. $PrP^{Sc}$ can enter the ER by retrograde vesicular transport and disturb normal folding and modifications or nascent $PrP^{C}$ proteins (see Figure 5). The ER thus serves as an additional site for $PrP^{Sc}$ amplification (Campana et al., 2005). Prolonged stress due to aggregate accumulation induces ER- mediated pro-apoptotic signaling, such as activation of ER-localized caspase-4 and JNK cell death pathway (Soto et al., 2012) (Li et al., 2006). Such signaling magnifies $Ca^{2+}$ efflux by triggering BAX/BAK dimerization on the ER membrane (Li et al., 2006).

## 1.5 Cytosolic and Nuclear Signaling Response to Reactive Oxygen and Nitrogen Species-Related Damage

14-3-3 proteins normally bind pro-apoptotic Bcl-2-associated death promoter (BAD) within the cytosol, preventing dimerization with anti-apoptotic protein Bcl-2. $PrP^{Sc}$ can be actively bound to 14-3-3 proteins, but it remains unclear what further activity is involved with this complex. 14-3-3 already makes up 1% of the brains soluble protein and its relative concentration is associated positively with increasing amounts of $PrP^{Sc}$ (Shi et al., 2014). 14-3-3 is an important regulator of normal cellular levels and modified states of BAD, Bcl-2-associated

protein 4 (BAX), and B-cell lymphoma 2 (Bcl-2). Sequestering of 14-3-3 by $PrP^{Sc}$ may decrease its ability to regulate apoptosis-associated proteins.

Excitoxiticity describes an excess amount of extracellular glutamate that causes overstimulation of respective receptors and commonly occurs in prion disease, as well as AD and PD. Glutamate binds N-methyl-D-aspartate receptors (NMDAR) which act as $Ca^{2+}$ channels. The resulting $Ca^{2+}$ influx and intracellular overload initiates as pro-apoptotic signaling response (Zhou et al., 2009). The calcium binds to calmodulin protein within the cytosol which then becomes an allosteric activator of nNOS, producing toxic amounts of nitric oxide (Zhou et al., 2009). In increased amount of glutamate in the extracellular space during prion infection may also cause damage to local oligodendrocytes and contribute to pro-inflammatory (M1) microglia activation (Amor et al., 2013). It's unclear exactly how prion infection is associated with excitotoxcitiy, but its likely decreasing concentrations of $PrP^{C}$ contribute to irregular release of glutamate at the synapses (Biasini et al., 2013). The ability of $PrP^{Sc}$ to infect cells other than neurons within the CNS opens up the possibility of damage to non-neuronal cells, like astrocytes. Normal function of excitatory amino-acid transporters (EAAT-2) also known as glutamate transporters on astrocytes can be disrupted by prion infection of the astrocyte. The loss of regular glutamate uptake by these transporters could be the major source of excess extracellular glutamate (Asuni at al., 2013).

Oxidative stress caused by the build up of ROS and RNS are associated with cellular signaling mediated by four major proteins: c-Jun N-terminal kinase (JNK), signal-regulating kinase 1 (ASK1), nuclear factor kappa-light-chain-enhancer of activated B cells (NF-κB) and forkhead box O3a (FOXO3a). ASK1 is an upstream regulator of JNK and NF-κB activity, thus JNK and NF-κB may be activated by some of the same signals (Mowla et al., 2013).

Products of such signaling include both pro- and anti-apoptotic factors. During low levels of oxidative damage and stresses induced by prion infection, such as $Ca^{2+}$ into the cytosol, the cell will attempt to alleviate stresses through upregulation of anti-oxidant response elements. The inability of the cell to reduce stress increases the strength of pro-apoptotic signals. The cell is unable the degrade $PrP^{Sc}$ aggregates, thus continuous generation of ROS and RNS as well as disruption of metal ion homeostasis inevitably drives the cell to apoptosis.

Essential components of apoptosis localize onto mitochondria to induce cytochrome c release onto the cytosol, which then contributes apoptosome formation and induction of apoptosis. Cytochrome c also aids $Ca^{2+}$ efflux from the ER. Mitochondrial cell death pathway requires the activation of BAX and translocation to the mitochondrial membrane. Other factors contributing to cytochrome c release includes Bcl-2 family proteins Bcl-2-like protein 11 (Bim), BH3 interacting-domain death agonst (Bid), and p53 upregulated modulator of apoptosis (PUMA) (Akhter et al., 2014). Bcl-2 itself inhibits apoptotic behavior (see figure 6).

Increasing amounts of reactive molecules cause enough damage to the mitochondria, ER, DNA, lipid membranes, and proteins that exceed the ability of built-in repair responses to handle the problems (Wong et al., 2012). Accumulated ROS and RNS generated through Harber-Weis and Fenton reactions, irregular oxidation events by involving loosely bound metal ions, and decreased Cu,ZnSOD function activates mitogen-activated protein kinase (MAPK) cascade (Uttara et al., 2009). Oxidative stress is also associated with excess amounts of cytosolic $Ca^{2+}$ due to ER stress and excitotoxicity, irregular glutathione cycling, slow loss of ATP and leakage of lysosomal compartments (Ölliger et al., 1995). Increased cytosolic $Ca^{2+}$ flows into the mitochondria through he $Ca^{2+}$ uniporter, interfering with their function, increasing reactive species, and contributing changes in membrane permeability transition pore and release of

cytochrome c (Kovacic et al., 1995) (Amor et al., 2013) (Xu et al., 2005) (Urrutia et al., 2014). $Ca^{2+}$ is an important regulatory signal under normal conditions, but excess amounts cause hyperactivity of calcium-binding proteins like calmodulin and calcineurin (CaN), which adds to apoptotic activity (Amor et al., 2013). Active CaN increases expression of nNOS and dephosphorylation of BAD, allowing it to dissociates from 14-3-3 and dimerization with Bcl-2 (Soto et al., 2012) (Shi et al., 2014). CaN also maintains unphosphorylated state of cAMP response element-binding protein (CREB) inhibiting expression of CREB-responsive elements TGFβ, BMP2, IGF-1, and IL-11 (Sinclair et al., 2013). Calmodulin binds nNOS and aids electron transfer for better nitric oxide formation (Xu et al., 2005). nNOS is also translocated to the mitochondrial membrane during high calcium concentrations (Carreras et al., 2007).

ER stress and reactive species influence nNOS expression through activation of NF-κB (Sinclair et al., 2013). NO weakens the integrity of the mitochondrial membrane and mediates apoptosis. Higher concentrations of NO decrease NF-κB activation through feed back inhibition (Carreras et al., 2007). Low levels of NO, as well as $H_2O_2$ (~20 $\mu M$) activate p38 MAPK. Higher concentrations and continuous signaling from NO and $H_2O_2$ induce apoptotic activity through JNK activation (Carreras et al., 2007). ER stress activation of NF-κB may initially mediate host defenses, but prolonged signaling will induce apoptotic signaling involving other key enzymes like PUMA, a target of p53 (Li et al., 2006). ER stress also activates local calpain proteases that then activate BAX and Bid as well as inhibit Bcl-2 (Xu et al., 2005). Dimerization of BAX and BAK on ER membranes aids efflux of $Ca^{2+}$ (Li et al., 2006). Excessive protein misfolding with the ER typically ends in cell death.

With the rough ER the protein BIP is normally bound to proteins ATF6, IRE1, and PERK. Misfolded proteins such as PrPSc that may have found its may into the ER matrix cause

BIP to dissociate from its normal binding partners in order to interact with PrPSc as part of the unfolded protein response (UPR). Unbound IRE1 and PERK then dimerize, causing self-phosphorylation and activation JNK, ASK-1, TRAF2, and EIF2alph, which selectively promote stress signaling (Todd et al.)

Early metal ion disrupted homeostasis caused Cu,ZnSOD to decrease by 50%, but an increase in MnSOD expression may compensate for loss in antioxidant protein during early infection (Sinclair et al., 2013). MnSOD tends to localize within caspase-positive aggregates in later infection stages due to damaged mitochondrial membranes (Sinclair et al., 2013). Approximately 6% of a chronically infected population of neurons fails to compensate for increasing concentrations of superoxide and other reactive species. Apoptotic cells may be recognized by externalization of phosphatidylserine (PS), which acts as a signal for phagocytosis (Sinclair et al., 2013).

Reactive species are also capable of oxidizing DNA base pairs within the nucleus (Jalland et al., 2014). DNA damage is associated with activation and accumulation of phosphoprotein p53 within the nucleus (Carreras et al., 2007) (Xu et al., 2005). JNK pathway signaling actually phosphorylates and promotes acetylation of inactive p53, restoring pro-apoptotic function (Sakaguchi et al., 1998).

Initial loss of $PrP^{C}$ may be compensated by increased expression of PRNP gene, and mediate damage associated with $PrP^{Sc}$ accumulation (Liu et al., 2013). Decreased levels of $Cu^{2+}$ correlate with upregulation of $PrP^{C}$ (Urso et al., 2012). $PrP^{C}$ expression is also negatively effected by active FOXO3a by binding to the promotor region of PRNP (Liu et al., 2013). FOXO3a also participates is expression of both pro-apoptotic proteins and enzymes involved in DNA repair and ROS detoxification (Huang et al., 2007). Insulin-like growth factor 1 (IGF-1)

promotes phosphorylated state of FOXO3a through the P13K-Akt pathway (Liu et al., 2013). FOXO3a is usually phosphorylated and bound to 14-3-3 within the cytosol in an inactive state. Withdrawal of particular cytokines IL-3 and -6 can trigger dephosphorylation of FOXO3a, dissociation from 14-3-3 and translocation into the nucleus (Akhter et al., 2014). JNK activated by oxidative stress and macrophage stimulating 1 (MST1) protein also promotes nuclear localization of FOXO3a. MST1 is typically upregulated during oxidative stress and may be modulated by active p53 (Huang et al., 2007).

Active FOXO3a within the cytosol promotes expression of Fas ligand (FasL) and tumor-necrosis-factor-related apoptosis ligand (TRAIL), which extrinsically participate in apoptosis by binding death receptors in the plasma membrane. Such signaling promotes activation of caspase-8 and formation of tBid and assisting cytochrome c release. Active FOXO3a also induces transactivation of Bim, a component contributing to mitochondria apoptosis, and expression of PUMA (Akhter et al., 2014) (Huang et al., 2007). FOXO3a can bind with Sirtuin-1 (SIRT1) a NAD+-dependent protein deacylase in the nucleus and then promotes expression of catalase and MnSOD to alleviate ROS (Hori et al., 2013). FOXO3a complexing with SIRT1 also prevents FOXO3a pro-apoptotic behavior (Hunag et al., 2007).

ASK1 activation can be stimulated by binding of IL-1$\beta$ and tumor necrosis factor alpha (TNF$\alpha$) released from pro-inflammatory glial cells to TNF receptors. ASK1 then promotes activation of JNK, p38 MAPK and other kinases that promote NF-$\kappa$B activity (Finkel, 2014) (Akhter et al., 2014). p38 MAPKs phosphorylate transcription factor C/EBP homologous protein (CHOP) and increase its transcriptional activity which inhibits Bcl-2 activity (see Figure 7). JNK also effects Bcl-2 levels by inhibiting its activation and aids apoptosis by phosphorylating and activating Bim (Akhter et al., 2014).

## 1.6 Activation and Migration of Local and Peripheral Microglial Cells

Prion infection is not limited to neuron but can also promote damage in glial cells within the CNS. $PrP^{Sc}$ has been found within the lysosomal compartments of astrocytes and microglia (Wojtera et al., 2012). The detailed impact of $PrP^{Sc}$ infection of oligodendrocytes (OLGs) and astrocytes are not detailed by this model, but their participation in infection by secreting signals promoting cell death in neurons and inflammation is. Secreted molecules and proteins include certain cytokines, growth factors, and regulatory enzymes (Lima et al., 2007). Neurons and surrounding glial cells have a dynamic exchange of signals that mediate their particular behavior. Neurons constituently express and release transforming growth factor beta (TGF$\beta$) that keeps microglia in a stable, normal state (Biber et al., 2007). Astrocytes release IL-4 that inhibits induction of phagocytic microglia. IL-4 also promotes expression of Ox-2 membrane protein ligand (CD200L) in neurons, which also maintain inactive states of microglia (Jurgens et al., 2012) (Wojtera et al., 2012). OLGs similarly express CD200L (Amor et al., 2013). IL-4 promotes microglial activity that repairs damage (M2) and increase secretion of IL-4, IL-10, and TGFβ (Peferoen et al., 2013). The exact mechanisms to induce pro-inflammatory states of microglia and astrocytes remain unclear, but activation in associated with the reception of distress signals from the damaged neurons like PS, certain cytokines, and glutamate (Urrutia et al., 2014). Activators of pro-inflammatory microglia response (M1) may also include UTP, ATP, IL-1β, and TNFα (Wojtera et al., 2012). M1 microglia produce a massive amount of inflammatory cytokines: IL-6, IL-12, TGFβ, TNFα, IL-1β, and IL-3 (See Figure 8). M1 microglia also generate NO and $\cdot O_2^-$ that mediate oxidative damage (Urrutia et al., 2014). Astrocytes also contribute to reactive species generation and extracellular accumulation following reception of TNFα, IL-1β, and IFNγ. Astrocytes secrete stress inducible protein 1

(STI1) which interacts with $PrP^C$ on neurons and promotes neuroprotective behavior by aiding CREB transcription activity (Lima et al., 2007) (Hartman et al., 2013). TNFα and IL-1β also enhance astrocyte expression of TNFα, IL-1beta, IL-6, and IL-4 (Wojtera et al., 2012) (Soto et al., 2012) (Urrutia et al., 2014).

## 1.7 Phagocytosis of Apoptotic Cell Material by Macrophagic Microglial Cells

Phagocytosis of apoptotic cell material requires direct contact between the macrophage and dying cell and takes approximately 3 to 6 hours to completely digest material (Witting et al., 2000). Of course digestion of PrPSc has its own limitations. Just as prion aggregates tend to be localized to endolysosomes, prion protein likely lingers in the digestive pathway with macrophages, slowing down the process of cell clearance. A number of receptors are involves in receiving apoptotic cells including CD68, CD14, and anexins, but reception of externalized phosphotidylserine (PS) has shown to be an essential step in the phagocytic process (Witting et al., 2000). Reception of apoptic material causes several enzyme cascades that contribute to cytoskeletal rearrangement and mobilization of calcium from endosomal compartments (Eichoff et al., 2011).

# Part 2: Creating an Illustrative Signaling Network of Prion Infection

CellDesigner is a visual tool used to represent biological reactions and processes using simple labeled shapes and arrows. We interpreted our findings and summarized them within CellDesigner files to create complicated systems as flow charts, which we then based our kinetic equations off of. Nearly all enzymes are organized into multienzyme complexes within the cell (Savageau, 2009). We attempted to reflect this fact by using complexes as they were understood from primary literature, but choose simplify many of the complexes to only include the components that performed a function outside of the complex following dissociation or activation.

## 2.1 Model One: Reactive Oxygen Species Generation During Prion Infection

Long before we attempted to deduce specific signaling pathways involved in prion infection, we first attempted to elucidate a general mechanism for the cell's death. The following is an image of our first model composed in CellDesigner software.

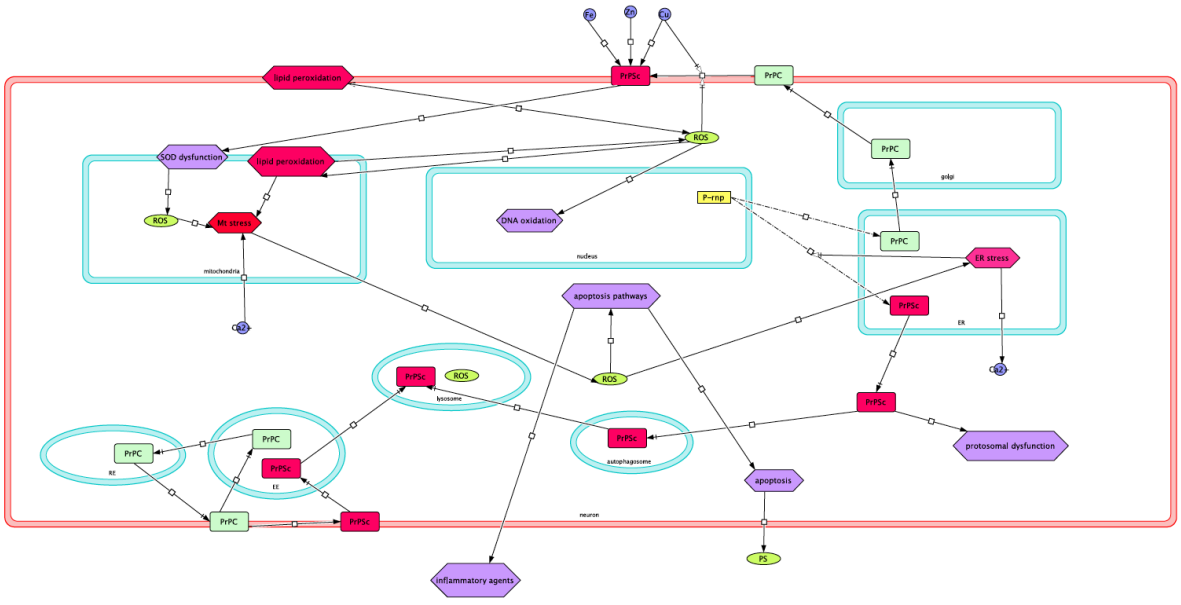


Figure 1. ROS generation and apoptosis during prion infection, a proposed mechanism for cell death.

From the literature we determined the amount of $PrP^{Sc}$ was related to the generation of reactive oxygen species. We also knew that $PrP^{C}$ and $PrP^{Sc}$ were trafficked to specific regions of the cell where they accumulate in aggregates and damage normal cell functions. In addition, we concluded that $PrP^{C}$ is capable of binding ions copper, iron, and zinc. We determined that $PrP^{Sc}$ through some unknown mechanism related to its ability to bind metal ions, was responsible for ROS generation in lysosomes and mitochondria. We also knew that cells experiences ER stress during infections, which caused release of $Ca^{2+}$ into the cytosol, but we were unsure of the significance that event would take on in our later models. We also concluded that prion protein inhibits the function of the proteasome system. We also found that $PrP^{Sc}$ indirectly induced lipid peroxidation as well as apoptosis though ROS generation. We had yet to propose a model that explained the causational relationship between $PrP^{Sc}$ and ROS generations and saw it as a major component of the disease.

## 2.2 Model Two: Whole-body Trafficking of Prion Infection

In our second model we decided to focus on the trafficking of $PrP^{Sc}$ throughout the entire body of an infected human. We concluded from the literature that initial replication of the lymphatic system of humans following ingestion of prion was most likely the main route by which $PrP^{Sc}$ first enters the brain. Unlike the first model, our second model, pictured on the next page, included multiple cells and even tissue types in the mechanism for prion proliferation. We don't intend to make the individual molecule identities discernable; the figure is for the purpose of demonstrating the extreme number of variables considered in that model.

In addition to extending the model to include multiple cells and areas where prion replication can occur, we included more specific pathways and activation of certain complexes

that will be explained with the current model. We decided not to pursue this model due to its extensive nature, and instead focused a model that described a cohesive story between prion infection at the surface of neuron to cell death. However, we wanted to incorporate the multicellular nature of infection shown in model two as well as the interactions between stressed neurons and local microglial cells, which can acquire a macrophagic phenotype and performs an specific role within the disease by phagocytizing apoptotic cell material.

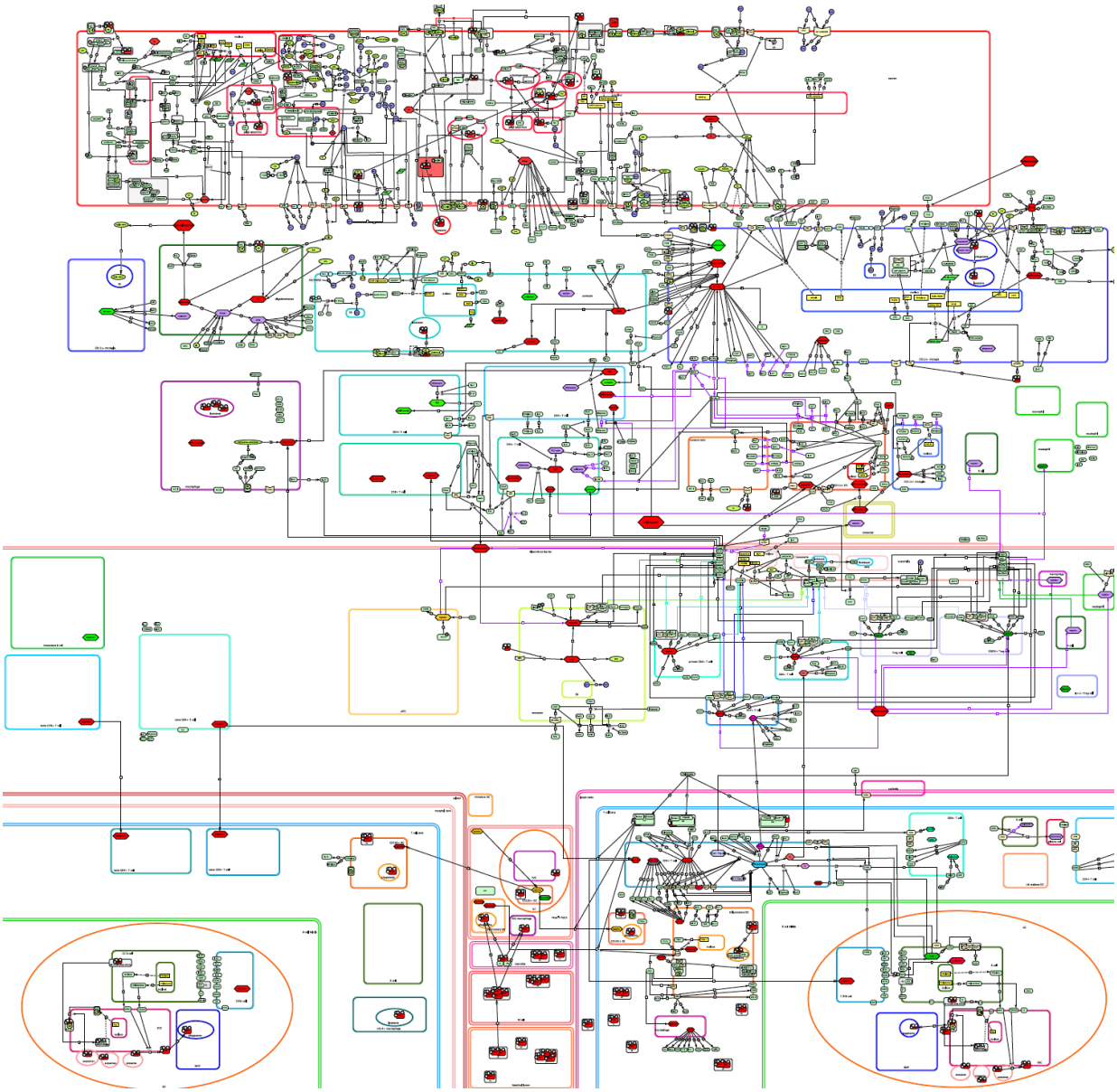

Figure 2. Whole-body Trafficking of Prion Infection, model two

## 2.3 Model Three: Trafficking of Prion Protein and Cellular Response to Prion Infection

We decided it was best to break down the model into four major areas that were designed as their own separate CellDesigner files. Combined they describe the trafficking of, damage induced by, and signaling response to prion infection of a single neurons and microglia. We won't disclose every detail of the model here, but the material in Part 1 discusses the majority of activities and reactions in the model.

### 1. Localization and Trafficking

We propose that $PrP^{Sc}$ first comes into contact with $PrP^{C}$ localized to lipid rafts with synapses. Prion conversions occurs were and $PrP^{Sc}$ invades the cell through $PrP^{C}$ normal endocytic cycling.

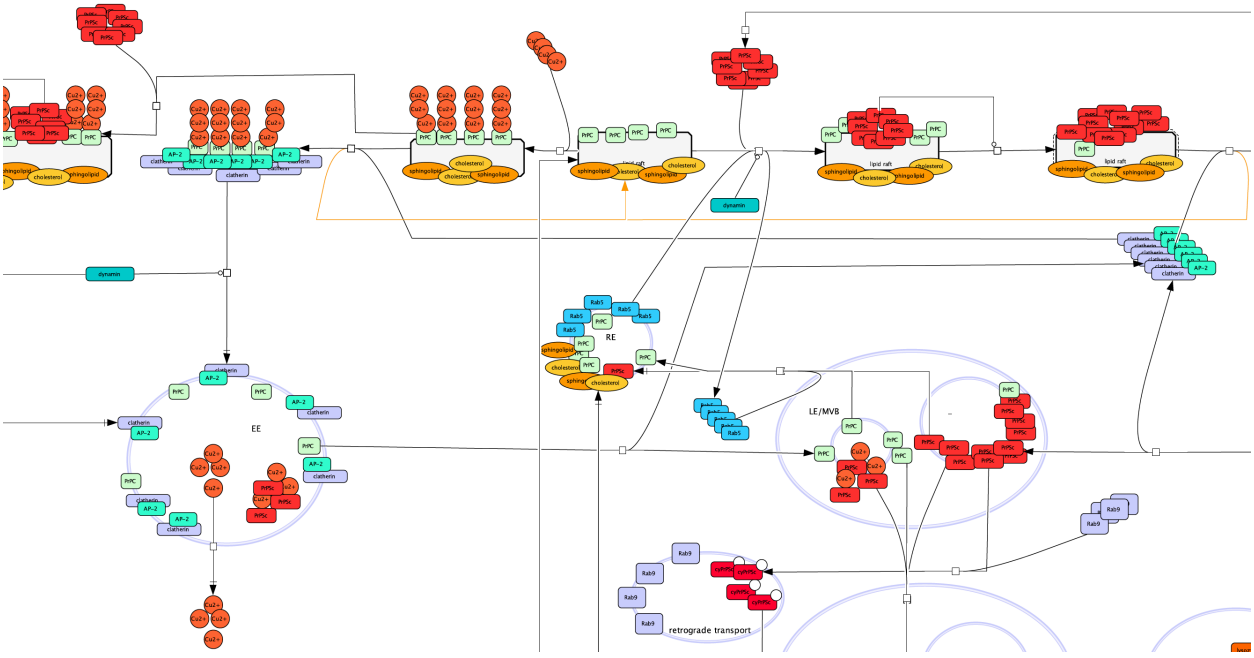


Figure 3. A CellDesiger representation of a synaptic terminal

$PrP^{Sc}$ continues to replicated with the cell's endosomal system until conditions within the cell deteriorate enough that undigested $PrP^{Sc}$ is released it the cytosol. Once in the cytosol $PrP^{Sc}$

aggregates are bound molecules meant to assist in the degradation of misfolded proteins. $PrP^{Sc}$ has been shown to be targeted toward autophagosomes, but avoid captures. Aggregates also deplete the cells proteasome system by occupying proteasomes that are unable to digest them.

Presented in the kinetic equations but not the CellDesigner file of the packaging of $PrP^{Sc}$ into exosomes and release out of the cell from MVBs. We propose exosomes are a significant mechanism of cross-infection between neurons.

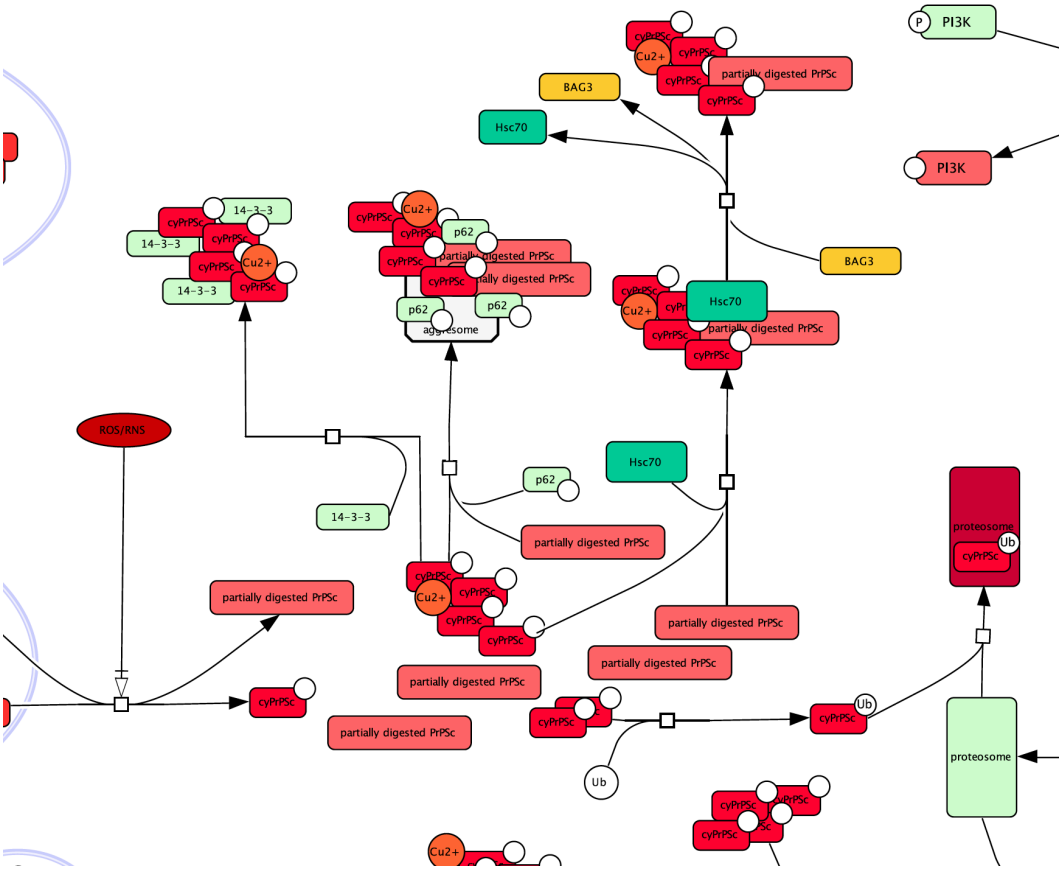


Figure 4. A CellDesigner representation of cytosolic $PrP^{Sc}$ binding activities

## 2. Mitochondria

Part 1 described $PrP^{C}$ natural affinity for copper ions and potential role it plays in proper copper homeostasis. Loss of $PrP^{C}$ could cause a depletion of copper in mitochondria and increased instances of ROS/RNS generation. There is additional depleted function of Cu2+ dependent SOD that decreased he cells capacity to handle excess ROS generation.

Included in this file is the signaling involved in mitochondrial membrane permeabilization by pro-apoptotic signals, resulting release of cytochrome c and activated caspase cascade.

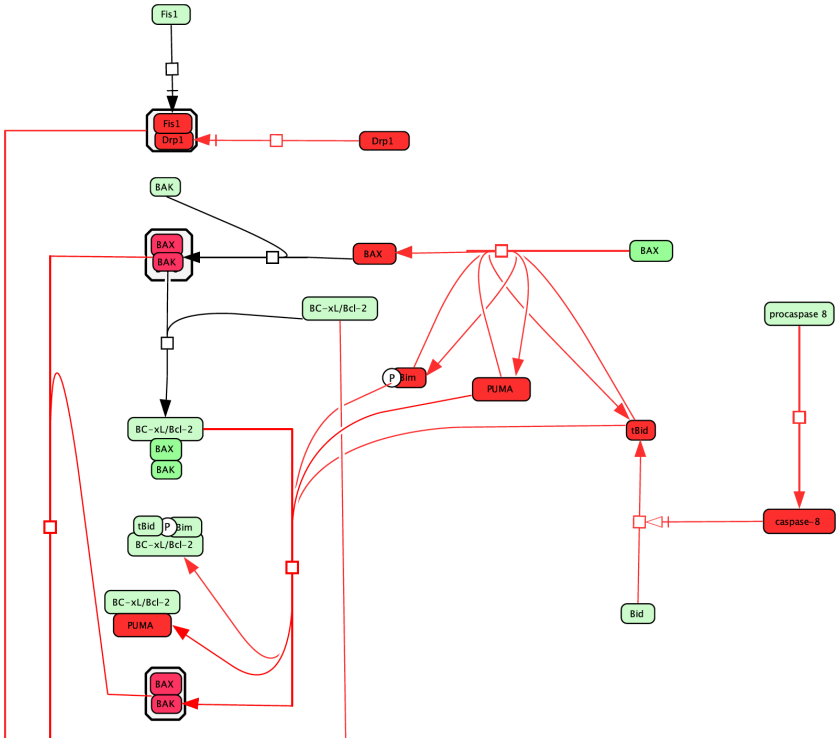


Figure 5. A CellDesigner representation of mitochondrial membrane permealization

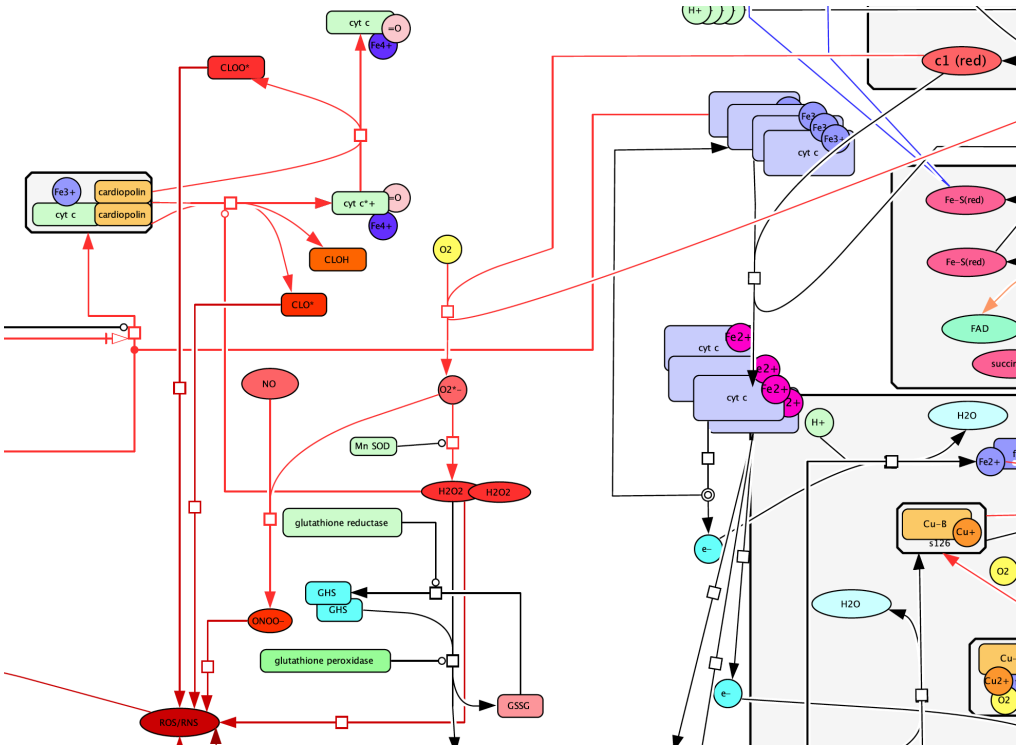


Figure 6. A CellDesigner representation of electron transport chain uncoupling and ROS production.

## 3. Nuclear and Cytosolic Signaling

Large signaling cascades in the model are initiated at the ER membrane, plasma membrane receptors and in the cytosol by ROS or RNS. Again much if this information is detailed in Part 1.

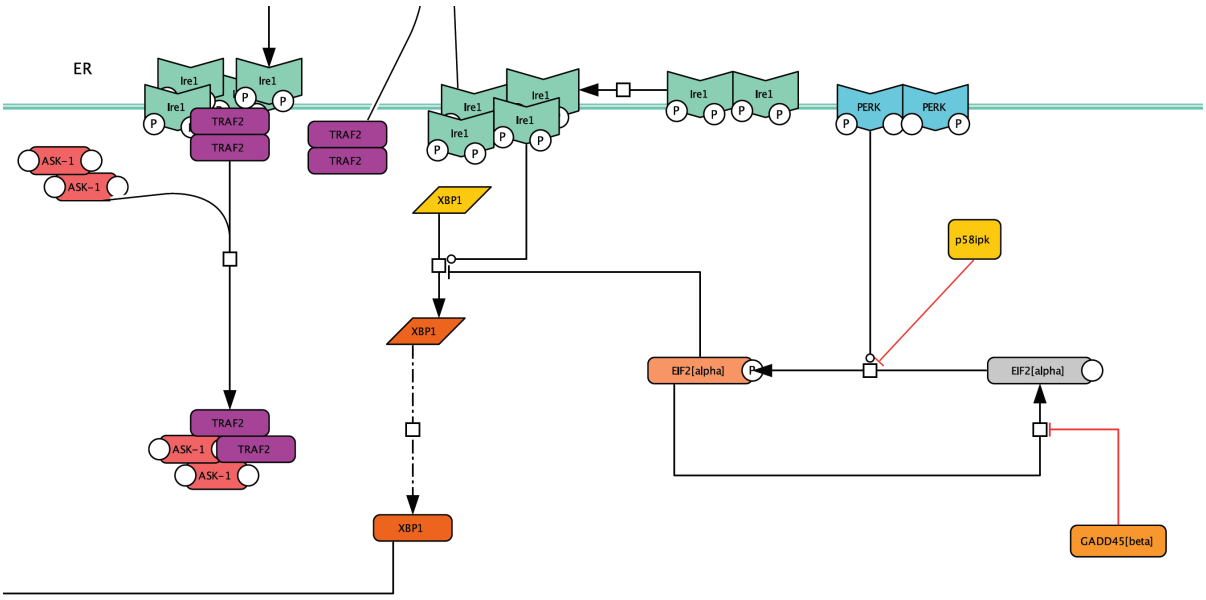

Figure 7. A CellDesigner representation of unfolded protein response in the ER

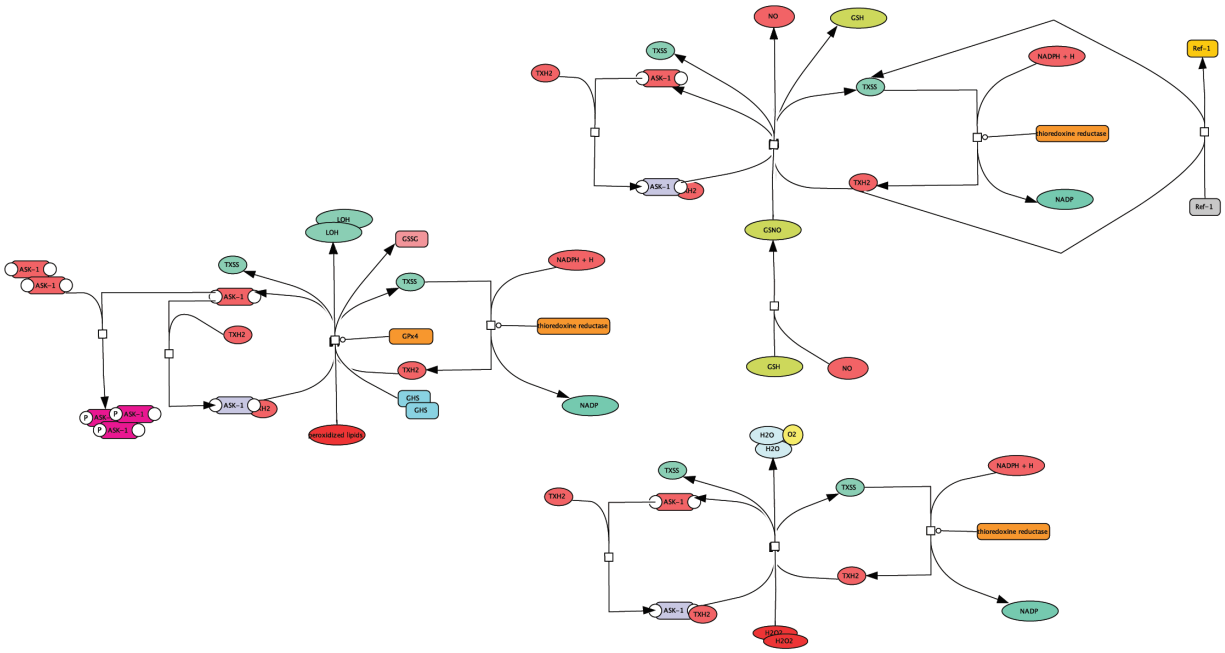


Figure 8. A CellDesigner representation of signaling directly activated by ROS

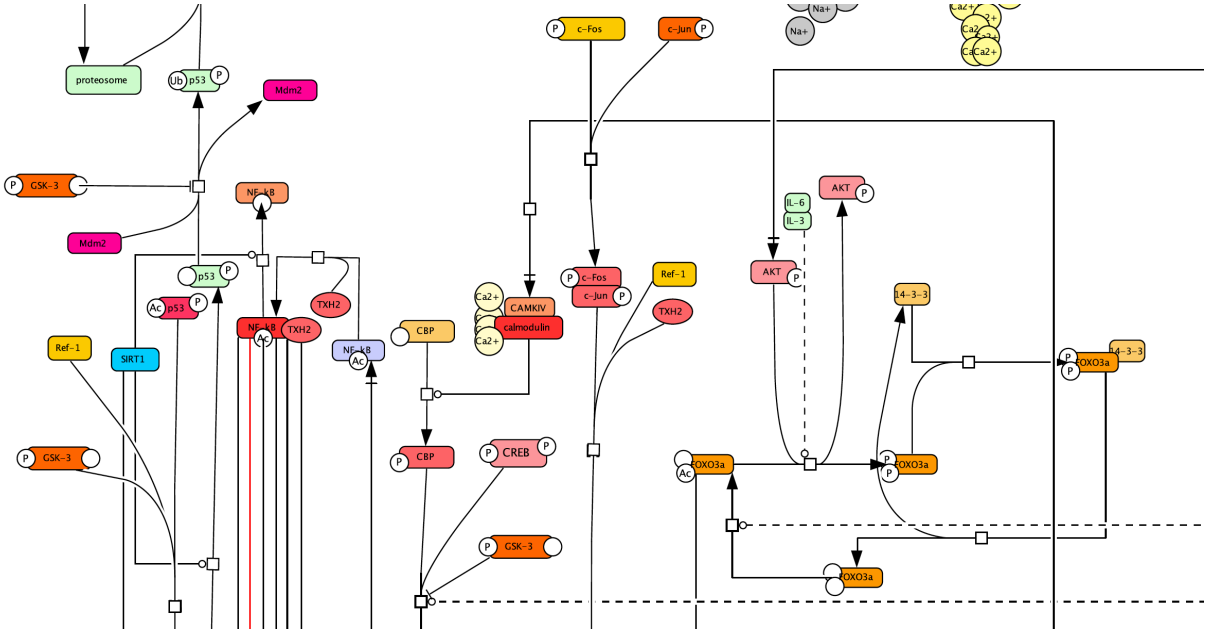


Figure 9. A CellDesigner representation of stress-related transcription factor modifications

## 4. Microglial Activation and Phagocytosis

The final CellDesigner file contains all of the reactions relevant to activation of microglia. Many of the same enzyme cascades present in neurons are shared by microglia, but are capable of inducing transcription of different mRNA than in neurons. This file also describes the binding of apoptotic cell material with the microglia's surface and subsequent phagocytosis and degradation.

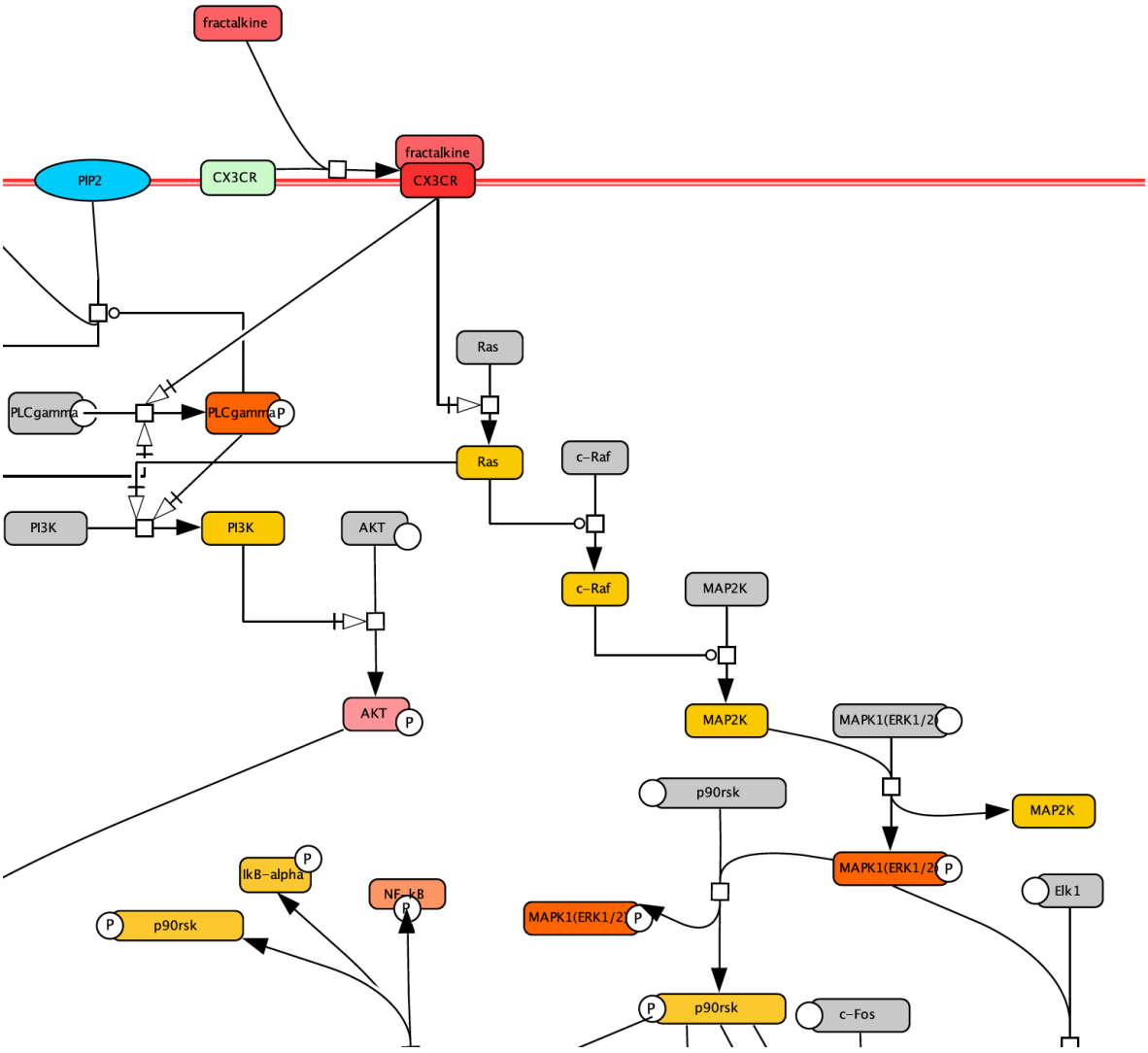


Figure 10. A CellDesigner representation of exogenous microglial phagocytic activation by fractalkine

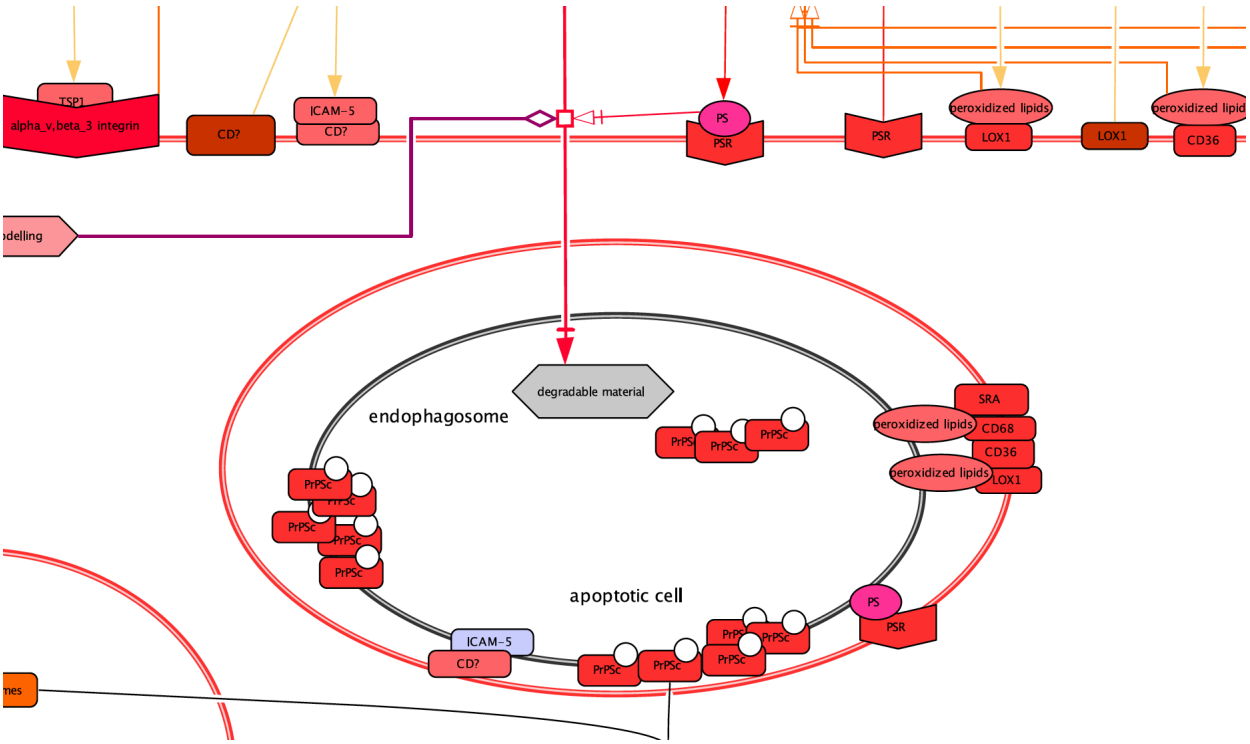


Figure 11. A CellDesigner representation of phagocytosis of apoptotic material

# Part 3: Coding Prion Infection as Sequential and Interdependent Kinetic Equations in Matlab

## 3.1 Explanation of Enzyme Kinetics

Biological reactions, particularly those involving enzymes do not often proceed via simple, sequential, and homogeneous linear first order reactions. Enzymes often interact with more than one molecule or biomacromolecule in order to perform their catalytic function. Additionally, in complex signaling networks, there may be instances of feedback inhibitions or activations as well as modulating molecules that place additional complexity on the system which often makes reaction rate equations high-order and non-linear (Savageau, 2009). We instead assume that reactions are first order with respect to each reactant. There may be a large number of reagents in a given reaction, which causes the order of the reaction to increase. If any of the individual reactants were an order higher than one, then it would become more difficult for the computer's algorithm to resolve in a reasonable amount of time. To making this approximation we linearize the rate laws for the reaction into a first-order system of equations. The equation must also be homogeneous, meaning they do not contain any terms unrelated to a concentration.

Consider the following representation of a simple signaling network, in which each variable $X_n$ denotes a generic reactant, product, and catalyst.

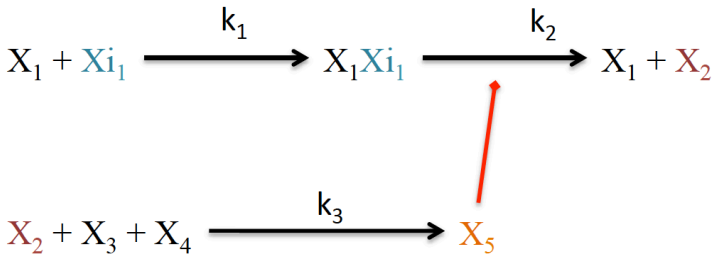


Fig 12. Sample Signaling Network

In the above example there is one instance of catalysis, one high order reaction, and one feedback inhibition. The rates of reactions are effectively lowered by the addition of a catalyst. We can adjust the reaction rate writing the rate in terms of its own differential equation, which is dependent on the concentration of the catalyst. The third reaction, which can be expressed in terms of a classic rate law, gives a third-order equation.

$$\frac{dX_5}{dt} = k_3[[X_2\ ]\ [X_3\ ][X_4]] \qquad (1)$$

Using our linearized approximations, we write the rate laws for the above products as follows:

$$\frac{dk_1}{dt} = \boldsymbol{k}\big[[X_1] - [X_5]\big] \qquad (2)$$

$$\frac{d[X_2]}{dt} = -k_1[Xi_1] \qquad (3)$$

$$\frac{dX_5}{dt} = k_3\big[[X_2\ ] + \ [X_3\ ] + [X_4]\big] \qquad (4)$$

We simplified the reaction catalyzed by enzyme $X_1$ with the steady state approximation so that the concentration of the $X_1Xi_1$ complex is constant and therefore not assigned a differential equation. If the formation of such an intermediate were involved in a separate reaction or fluctuating, then we would write the reaction as a classic rate law. Instead we wrote the reaction rate as its own differential equation. The change in rate over time is equivalent to some constant ***k*** multiplied by the catalyst minus ***k*** times an inhibitor. In this reaction $X_5$ acts as a feed back inhibitor and decreases the rate of the reaction. In a general definition, the change in a variable's concentration is a sum of the rates of reactions in which the variable of interest is the product minus all rates in which the variable is a reactant (Savageau, 2009). For the purpose of our project we input a large set of rate laws using this format into coding software, and then use that software to solve all of the equations to obtain the rates and concentrations at a given time.

The greatest assumption underlying biological systems modeling is that we can apply the same physical and chemical laws to reactions occurring within a cellular environment. Enzymes are the biological catalysts that lower reaction energy barriers or the activation energies ($E_A$) in order to produce forward reactions that under normal biological conditions would not occur. Just as catalysts are reproduced in the end of any given chemical reaction, an enzyme needs to return to its original state following the reaction. Mass must also be conserved during the reactions, and the reactions must obey the general laws of mass action just like traditional chemical equations.

It is not only the reagents that have to obey these laws. Catalytic reactions may themselves be modeled as differential equations and then solved at the same time as the equations representing concentrations. The rate of catalysis below a saturation threshold can be affected by the concentration of the catalyst, and it is therefore important to change the rate as a function of the catalyst concentration.

## 3.2 Why Use Matlab?

It has only been in the most recent decade that scientists have shown a renewed interest in synthetic biological systems. Many of the mathematical assumptions I use in my model have actually been derived and used for over 100 years; it is only now that readily accessible computational software has become available that has the capacity to carry out complicated analysis on a large scale. Matlab software is a flexible coding environment that is equipped with an endogenous library of accessible functions known as toolboxes that can be used to manipulate imputed date. One particular function, known as an ordinary differential equation (ODE) solver, has been of particular use to this project. The ODE solver accepts an input matrix of written differential equations, and produces a matrix of solved equations for each time step specified in

the solver. This matrix of concentrations can then be plotted as a function of time, yielding a graph of the change in species concentration over time, for any specified number of species.

Matlab is a matrix-based computer language, and is capable of storing large amounts of data. My model requires tracking over 700 variables for every neuron, not including the synapses and specified locations of certain species for each time step. If we wanted to model 10 neurons and their enzymatic behavior over only 100 seconds it would require software that can effectively store greater than 6 million values, in such a way that we could easily access every value using a simple index system. Matlab was adapted for use in our lab only within the past two years and has proved sufficient for handling such large data sets.

Matlab was originally designed to help engineers design physical systems, but has been adapted for a number of applications, including biological systems analysis, and now includes specific toolboxes that alleviate the laborious task of writing novel code for a general biological system. We however choose not to use any of Matlab's SimBiology toolkits, in order to preserve the uniqueness of our system. The Matlab language is extensive enough that we can compose our own library of functions, write equations using conditional statements, and make any number of changes to our code or initial parameters to fit what we desire. Most importantly, we can change how often our code is run, which allows us to manipulate the time scale of the model as well how many cell systems are run at a time.

One limitation in using computers to solve complex signaling networks is that it presupposes the long-term behavior of enzymes that would ordinarily be determined by extensive real kinetic studies (Savageau, 2009). We can attempt to counter this limitation by incorporating conditional statements into the set of differential equations, such that if the system encounters certain conditions it will alter the behavior of functions based on specified

instructions within the statement. Here is one example from the Matlab script containing all of our rate law equations:

```
if X(15)/X(1) >= 1;                          %PrPSc aggregates are endocytosed spontaneously
  dX(15) = X(756)*X(1) - K(1)*X(15);          %total surface PrPSc
  dX(53) = K(1)*X(15) + K(1)*X(65) + K(1)*X(66);  %PrPSc/AP-2/clatherin
  dX(65) = - 2*(K(1)*X(65));                  %free clatherin
  dX(66) = - 2*(K(1)*X(66));                  %free AP-2
  dX(313) =  2*(K(1)*X(555));                 %total available sphingolipid/cholesterol
                                              %surface
  dX(555) = - 2*(K(1)*X(555));                %total sphingolipid/cholesterol LR

elseif X(15)/X(1) < 1;
  dX(15) = X(756)*X(1);                       %total surface PrPSc
  dX(53) = 0;                                 %PrPSc/AP-2/clatherin
  dX(65) = - K(1)*X(66);                      %free clatherin
  dX(66) = - K(1)*X(66);                      %free AP-2
  dX(313) =  K(1)*X(555);                     %total available sphingolipid/cholesterol
                                              %surface
  dX(555) = - K(1)*X(555);                    %total sphingolipid/cholesterol LR

end
```

In the above code, the 'if' clause (bold) considers the current concentration of surface $PrP^{Sc}$ and runs the code modeling initiation of endocytosis only if the ratio of $PrP^{Sc}$ to $PrP^{C}$ exceeds one. Otherwise, the 'elseif' statement runs the equations not involving $PrP^{Sc}$ endocytosis if the ration is below one.

To conclude, Matlab is an excellent choice for biological systems analysis for its ability to store enormous amounts of information in easily accessible matrices, the robustness of its ODE solver, and the flexibility of its language that allows conditional treatment of differential equations as the simulation runs.

## 3.3 Assumptions Taken in Writing Kinetic Equations in Matlab

We have already spoken briefly on the general chemical and physical assumptions taken when modeling biological systems, but there are additional assumptions taken in order to accurately depict chemical reactions in code.

Even though there are now extensively populated databases for proteins, genes, and biological reactions, it is difficult to find concentrations for every reagent in the model. Harder still is finding literature values that have been derived from the same model system, produced under similar conditions, or even derived from the same tissue. It is therefore not useful to use only the pure values from databases. Alternatively we have, in the past, approximated the initial concentrations as well as the initial reaction rates in order to have the model produce kinetic results in which the concentrations are at least in relative proportion to what would be found in nature. These approximations are completed using a system of trial and error by changing the initial conditions until the output fits the expected ratios, rendering the initial concentrations as essentially arbitrary fitted values not directly related to real biological systems. The final values could them be multiplied by some empirically derived constant in order to obtain the final concentrations in line with realistic biological values. This has worked in the past to produce beautiful results by revealing trends in the disease state, however it violates our goal to generate the final model using bottom-up design.

Our approach was to find as many values for variables that were derived from cells taken from the human cerebral cortex or neocortex, and then scale those values so that they were at least within a similar order of magnitude. For values we could not find in the published literature, we approximated them as one times the order of magnitude calculated for the found values. That way all of my values were within a certain range of magnitudes, which was derived from actual literature.

A second assumption is that all initial concentrations are not the same for each cell type. As will be explained in greater detail in Part 3, neurons in this model take on different phenotypes, which can vary extensively in their internal volume and surface area and therefore

molecular concentrations. We thus additionally scaled a given neuron's initial concentration values relative to the phenotype with the smallest average internal volume, the L2 pyramidal neuron.

Without concrete spatial information about the distribution of cells, we assume molecules and macromolecules are distributed uniformly within the cell with the exception of $PrP^{C}$, $PrP^{Sc}$, and interacting molecules, which are tracked as they evolve through endocytic vesicles. In reality, most biological reactions are localized to certain areas of the cell. We have attempted to replicate the compartmentalization of certain reactions that may be occurring in different environments by writing differential equations for each specified location. For example, SOD1 is localized to both the matrices of mitochondria and the cytosol. It was important that these enzymes catalyze reagents specific to their location, and so we wrote them as two different equations.

We first assumed in the kinetic model that the spread of prion infection from neuron to neuron is related only to the concentration of $PrP^{Sc}$ released in exosomes, meaning that the concentration of $PrP^{Sc}$ is received by a given neuron is related through a differential equation containing the total concentration of $PrP^{Sc}$ in exosomes released from each neuron. In reality, $PrP^{Sc}$ likely spreads in a spatially dependent manner rather than through an immediate uniform distribution. We then attempted to incorporate a pseudo-spatial component by making the concentration of $PrP^{Sc}$ received by each neuron at a given time inversely proportional to the difference between the index of the one infected neuron and that of another given neuron. Essentially, the greater the difference in the neurons' index values, the less $PrP^{Sc}$ is received from the exosomes of the infected neuron. Exosomes come into contact with receiving cells by direct fusion with the plasma membrane or by endocytosis and their content released directly

onto the surface or within the MVBs. Therefore, half of the received amount of $PrP^{Sc}$ was assigned to be localized on the receiving neuron's surface, and the other half to the MVBs. We were unable to determine how often an exosome would be endocytosed or fuse with the plasma membrane and therefore used a 50:50 approximation. This method was extended to incorporate other variables that are exchanged between cells including soluble ligands.

Not much information exists yet on termination of certain types of signaling molecule activity. Unless a specified mechanism of deactivation such as proteosomal degradation or subsequent reactions with other regulatory enzymes, deactivation was modeled as a simple first order reaction to reform the original molecule. This produces a quasi-steady state of certain variables.

Even though we have attempted to include as much detail as possible, our proposed signaling network does not include a reagent for every reaction. We tried to incorporate general trends in results from literature. If a concentration or presence of certain molecules may only have been related to a result we show that relationship through a general causation mechanism. The rate of such an event is then written as a differential equation similar to a catalytic reaction. Alternatively, we wrote several reactions involving unknown molecules to 'fill the gaps' in certain mechanisms.

## 3.4 Applying Kinetic Equations to More Than One Cell

Once we had established the set of differential equations describing every concentration and reaction of interest the next challenge was to expand the simulation beyond a single cell case. Matlab has several ODE functions within its library capable of solving differential equations, but some are more applicable to solving linear, first order equations. We chose to use

the ode15s solver which was specifically designed to handle stiff differential equations of variable order, meaning it uses a variety of numerical methods to solve the equations in order to give a closer approximation to the solutions, and is capable of solving for equations of different order. By virtue of being designed to handle stiff equations, it is better for solving equations, the ode15s solver is better for solving  involving larger numbers of reactants, like those used in our model.

The ode15s solver accepts a single vector-column matrix containing differential equations, a time span, and a single vector-column matrix containing initial values as input. It outputs a single vector-column matrix of time steps and a 2-dimensional matrix of species concentrations over time. This is a problem when one wants to solve multiple sets of equations at once. This posed an additional problem as neurons naturally exchange molecules through synapses and concentrations need to reflect this exchange but would not be able to if each set of equations were solved individually. As I mentioned earlier, Matlab can store large amounts of data in arrays or matrices. In order to solve the kinetic equations I stored all initial values in a three-dimensional array we called ‘neurons’. The first dimension was time, the second was reserved for the concentration of a given variable, and third was a length equivalent to the number of neurons. Essentially it was the 2x2 matrices containing the initial values for each neuron, stored as one matrix. I then wrote what is called a ‘for loop’ which causes the code containing the ode solver to repeat a designated number of times and set the ode solver timespan to one. By making the loop iteration equivalent to the time span, we feed a set of initial values from our neuron matrix into the solver, as well as the set of differential equations, stored the solved solutions in the same neuron matrix at the appropriate time index and set it so the most recent solved values became the initial values imputed into the solver upon the next iteration. We

actually created a ‘double for loop’ such that every time the code was run, the ode was run to solve the equations for every neuron’s most recent solved values, for each time step. Once the code compile, we had a populated three-dimensional matrix containing the concentrations of each variable for each neuron at each time step and we could then plot the values as changes in concentration versus time.

We used a similar method to store and solve for the variables of interest for microglial cells. We created a similar three-dimensional matrix called ‘microglia’ and iterated over its values within the same loop as the neurons matrix. However, the behavior of microglial cells is highly dependent upon the activity of neurons and it was therefore necessary to incorporate simultaneous solutions from the neurons into the microglial equations. We also return to earlier mentioned problem that the ode certain variables are also shared among neurons. At the beginning each time loop, we sum over certain variables within the neuron matrix so that I get total values for each. We wrote these totals as concentrations by dividing the total by a volume associated with the given number of neurons. These new total concentrations were then stored as the ‘initial’ concentrations for dependent variables in the matrices and imputed in the solver during the iteration to be used in the differential equations for certain process involving extracellular signaling.

## 3.5 Results of Kinetic Model

After completing the code for the pseudo-spatial model we were able to successfully generate three-dimensional arrays containing the concentrations of dependent variables from our solved equations. The resulting plots of these values over time revealed interesting and complex

behaviors. As seen in figure 13 and others we observed nonlinear growth and decay of concentrations for nearly every variable in the model.

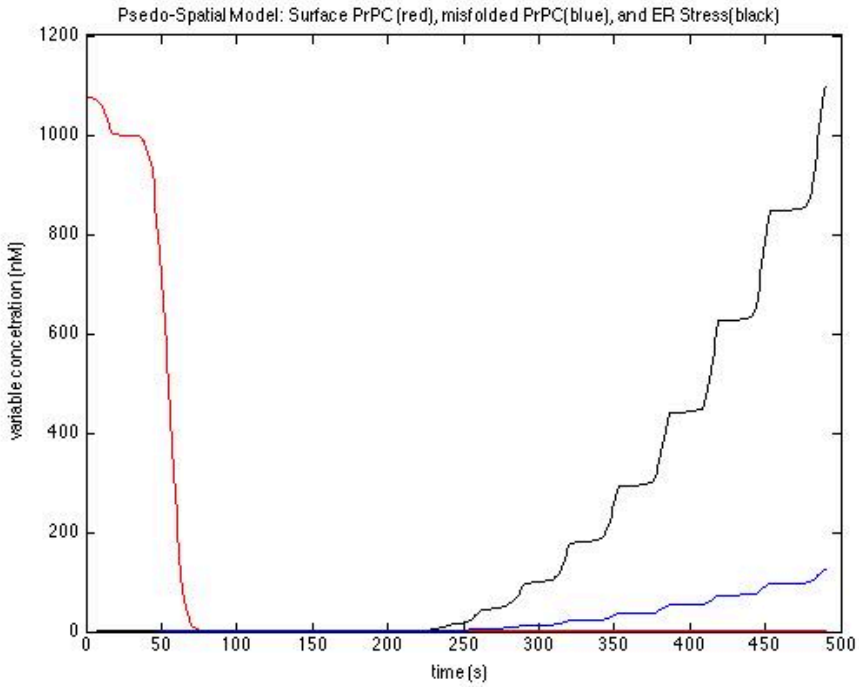


Figure 13. A plot of concentrations corresponding the $PrP^C$ contained in lipid rafts, misfolded $PrP^C$ in the ER, and ER stress

We expected to see a general decrease in the total amount of $PrP^C$ and increase in phenotypic values derived from the concentrations of variables contributing to stressed conditions, such as ER stress, but we did not foresee the step-wise exponential change in many of the variables. In figure 13, the decrease in $PrP^C$ appears to correspond with an increase in ER stress and therefore increase in nascent $PrP^C$ misfolding events. We suspected the stepwise behavior was a result of the endoyctic trafficking of PrP protein. The steps appear to increase smoothly over time and we expect that increase to corresponding to the concentrations of $PrP^{Sc}$ being localized in the ER.

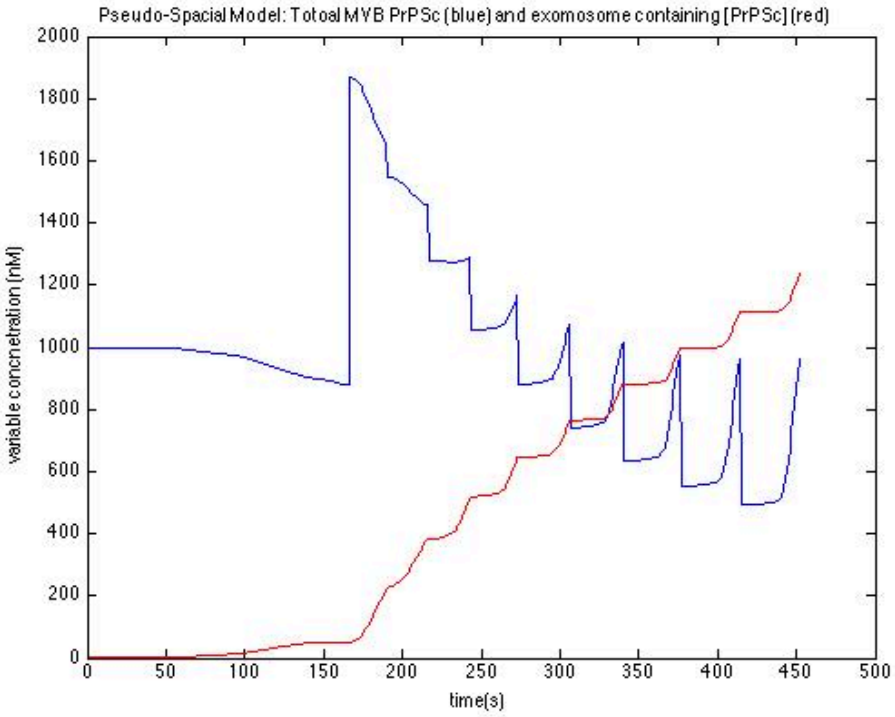


Figure 14. A plot of concentrations corresponding to $PrP^{Sc}$ in MVBs and in exosomes

From the above figure #, we were able to determine some interesting oscillatory patterns in the amount of PrPSc contained in MVBs. We suspected that as the number of early endosomes target toward MVBs increased during the disease state, it would overwhelm the MVBs capacity to traffic them to internal compartments. From literature we learned that neurons show increase exosomal release during prion infection. We believe Figure 14 reveals this expected behavior.

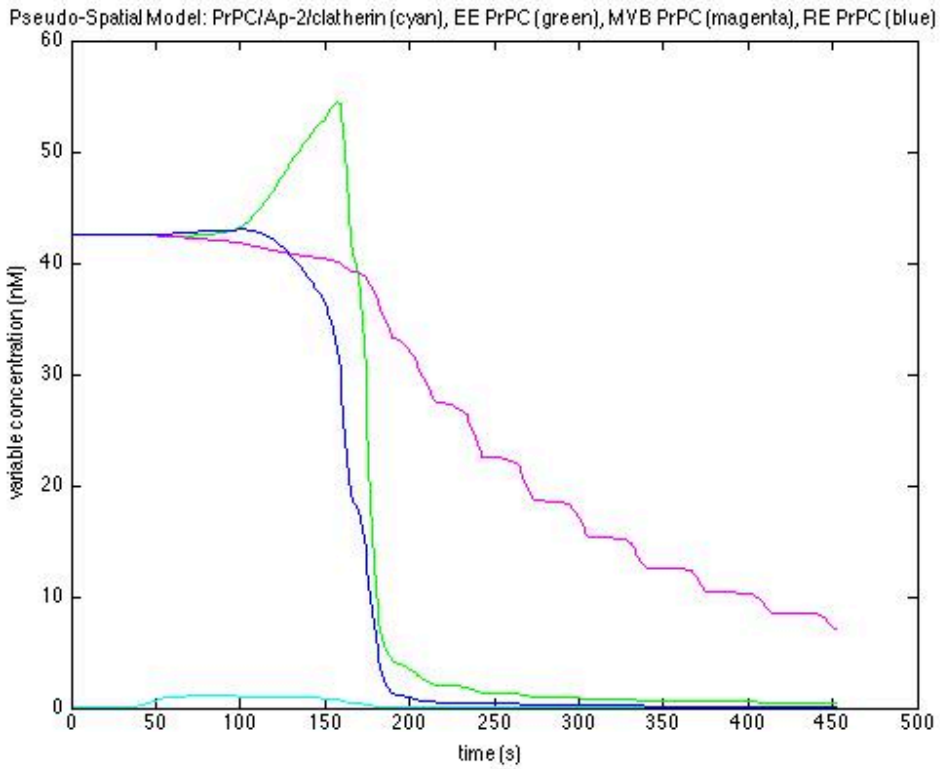


Figure 15. A plot of concentrations corresponding to displaced surface, early endosomal, MVB, and recycling endosome $PrP^C$

Under normal conditions we observed a stable concentration of $PrP^C$ in each of its localizations, however, upon arrival of prion protein we saw decreased recycling of $PrP^C$, a decreased about of displaced surface $PrP^C$ which likely a result of the overally decrease in surface $PrP^C$, and a slow decrease in the amount of $PrP^C$ in MVBs. We were curious to see the sharp increases in the concentration of early endosomal concentration and even sharper decline. Some literature values indicated increased frequency in endocytosis during infection, which offers an explanation for this pattern.

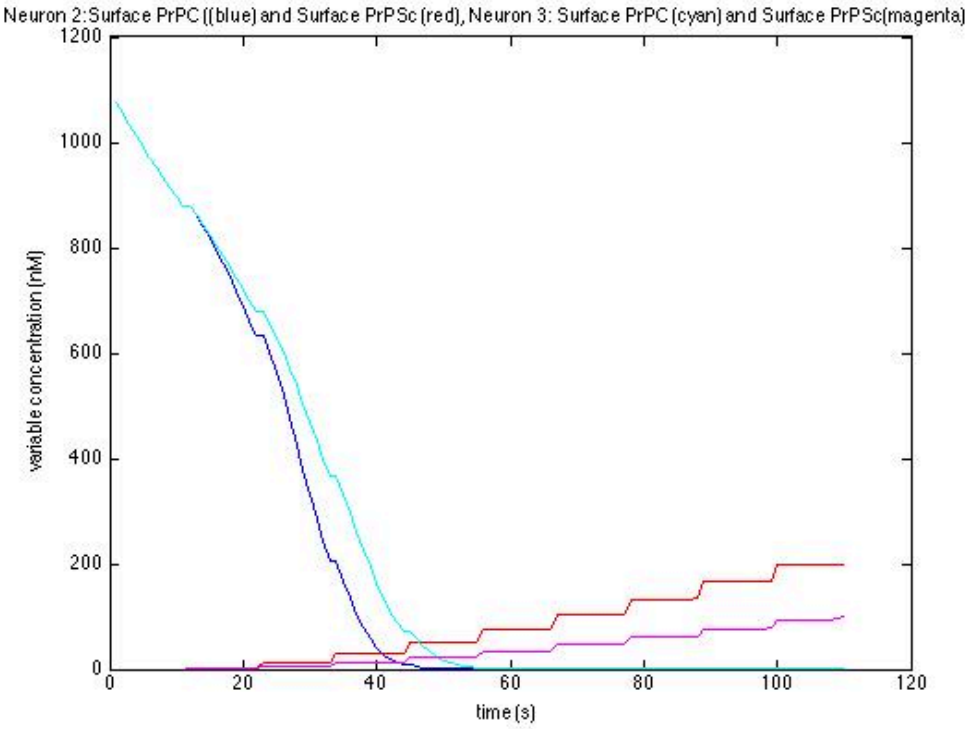


Figure 16. A plot of concentrations corresponding to surface $PrP^{C}$ and $PrP^{Sc}$ for two neurons

We were able run the equations on a multicellular system as well. As explained in the previous section, we modeled prion infection as mainly occurring through release and capture of exomsome containing $PrP^{Sc}$. These exosomes likely infect the closest neuron to its parent cell, we were able to vary the concentration of $PrP^{Sc}$ received by each neuron based on their 'distance' from the originally infected neuron. The results the second and third neuron in the model revealed slightly off-set similar behavior. The values for $PrP^{C}$ began to decline later for neuron three, which gave us an indication that our pseudo-spatial component was working.

We are still working our way through every variable in the model to analyze its behavior; there are a large number of correlational variables that still need to be plotted together so that we can interpret more details of the disease state. We also plan to manipulate some starting conditions such as initial $PrP^{Sc}$ concentration, as well as multiple initial sites of infection in order to explore the number of disease states that result from this single model.

# Part 4: Generating a Spatial Approximation of the Human Neocortex in Matlab

## 4.1 Cylindrical Approximations of Neurons

Neurons have extensive morphologies that create a unique space in which each cell is interacting with nearly every other cell within its vicinity through its axonal and dendritic branches. The crowded nature of the neocortex makes it a fertile environment for prion infection because $PrP^{Sc}$ cannot only be exchanged through exosomal release and capture, but can also reach across synaptic junctions, which number in the hundred thousands for typical CNS neurons. A model that can represent the overlap of branches would be difficult to construct in Matlab, and even if it were possible, the model would exceed Matlab's capacity to carry out multicellular simulations involving a direct three-dimensional representation of neurons. In order to simplify the neurons complexity but retaining their overlapping quality, we tried to describe the volume occupied by the neurons' branches and somas in terms of basic shapes and plotted them within a small volume that represented the grey matter's average depth (1800 μm white matter to pia). These shapes could be fitted using certain parameters derived from literature that describe the morphologies of specific phenotypes.

We used the following phenotypes in our model, listed from shallowest to deepest depth, where the letters and numbers correspond to certain regions of the grey matter depth: L2 pyramidal (L2py), L3 pyramidal (L3py), L4 star pyramidal (L4sp), L4 spiny stellates (L4ss), L5 slender tufted pyramids (L5st), L5 thick-tufted pyramids (L5tt), L6 cortical pyramids (L6cc), L6 corticathalamic pyramidal (L6ct), and L6 inverted pyramidal (L6invpy). These are only a few of the many neuronal phenotypes within the neocortex.

Our first assumption was to model neurons as boxes. Boxes can easily be generated using Matlab code, and then displayed to show the overlap of branch volumes. Each neuron to be generated was randomly assigned a phenotype, and then defined using the corresponding set of parameters, which included the maximum lengths of apical, basal and axonal branches.

It was also easy to determine the approximate volume overlap of branches between neurons, which would then be used to determine the likely number of synapses formed between the neurons with overlapping regions. Microglia could similarly be modeled using boxes having more uniform dimensions, but the internal special conditions of glial cells has not been an area of focus in my project. Microglia exist in an irregular ratio with neurons in different regions of the brain. Though the actual ratio remains obscure, average values tend to give a 1:2 ratio between glia and neurons. For any specified number of neurons generated in the special model, a number of local microglia and peripheral precursors related to this ratio were generated, assigned coordinates within the bounds of the system, and visualized as stars of size unrelated to natural proportions in the three-dimension representations. We scaled the coordinate system in which the cells are plotted so that 25 μm is equivalent to one unit in the representation. In order to prevent overlap of the neuronal somas, the coordinates of each neuron were assigned so that they were at lease 30 μm apart. The cell bodies within the neocortex tend to lie within 50 μm of each other and as a consequence of this natural crowding, when enough neurons are plotted in a sample volume such that it reflect the natural cell population, each neuron falls within 2 units or 50 μm of its nearest neighbor.

In a separate Matlab script we attempted to assign the initial locations of $PrP^C$ at synapses and within endocytic compartments. The distribution of the total [$PrP^C$] was defined empirically and had no basis on the actually synaptic placement and distribution of $PrP^C$. The images below

were generated using three separate scripts to plot the neurons as boxes and their localized $PrP^C$ as different colored and shaped points. The red represents the volume occupied by axonal branches, the blue is the volume occupied by dendritic branches and the small green box in the center represents the soma.

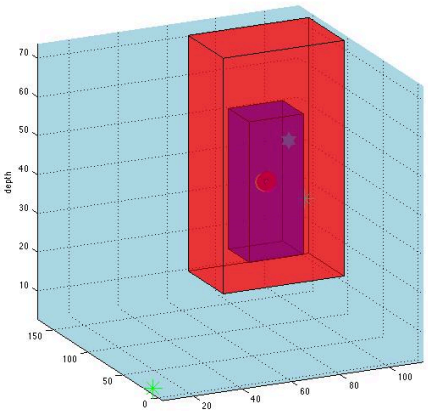


Figure 17. Representation of one neuron with plotted $PrP^C$ populations

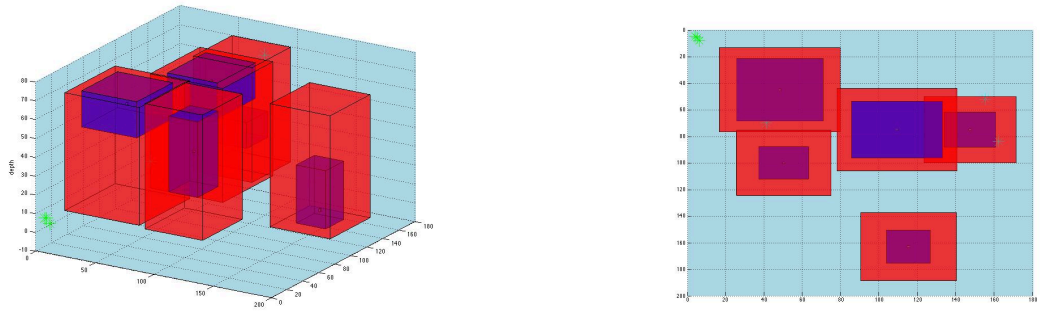

Figure 18. Representation of five neurons with plotted glial cells (green stars) viewed from an angle (left) and from the top (right).

The greater the number of neurons plotted within the same volume the more overlap between the volumes occupied by branches. At high cell densities it becomes nearly impossible to visually distinguish between the plotted neurons.

Even though using boxes as models for neurons provides an easy way to determine overlap it does not accurately reflect the radial symmetry of neuronal branching. The boxes also give no information regarding the relative density of branches within regions of overlap. We defined the density of branches as a dimensionless value given by the following ratio:

$$\frac{volume_{\ branches}}{volume_{total}} \qquad (5)$$

If a small area within the overlapped regions has a high density of branches for both neurons it is then likely that the axon of one forms a synapse with a branch of the other.

## 4.2 Visualization of Cylindrical Approximations

Cylinders, unlike boxes are capable of approximating the radial symmetry of neuronal branching, and can also describe the depth or vertical length of a single neuron's volume projection. However, the cylindrical approximation still does not accurately depict the morphology of branching, and therefore cannot be used on its own to describe the branch densities. Cylinders also make it more difficult to determine the coordinates of the overlap volume between neurons, as their geometry is more complex.

We used code similar to that used to generate the boxes to define the cylindrical representations. We also wrote the code so that it receives a range of integer values that will be used to define the bounds of a semi-random number generator to determine the number of neurons and glial cells plotted within the sample volume. This added another stochastic element

to the model so that a different environment can be generated each time within the parameter ranges derived from literature.

The following are images of the cylindrical approximations. The pink cylinders correspond to the axonal branch volumes, the yellow cylinders correspond to the dendritic branch volumes, and the cyan or red spheres correspond to the somas of each neuron.

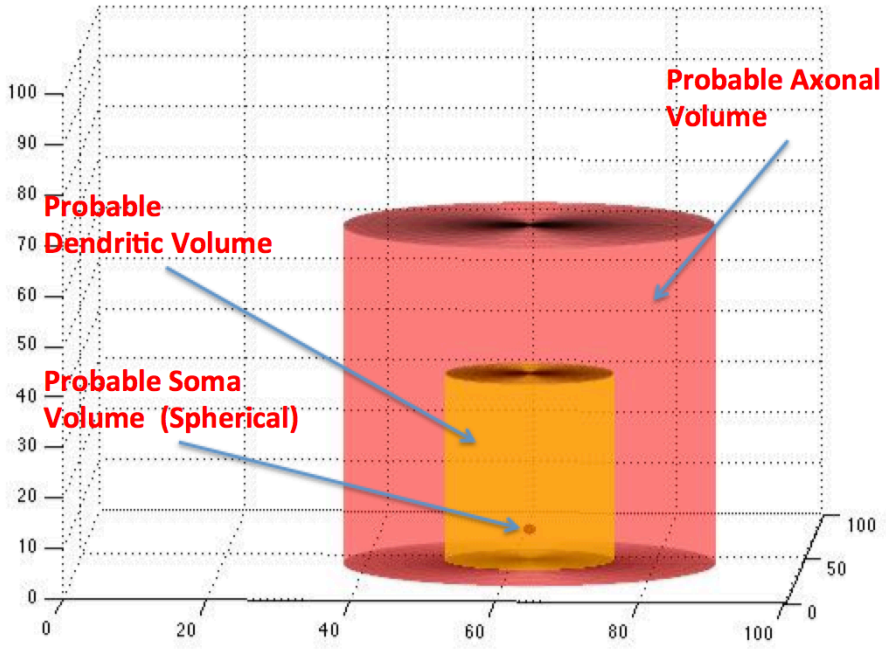


Figure 19. A cylindrical approximation of one neuron

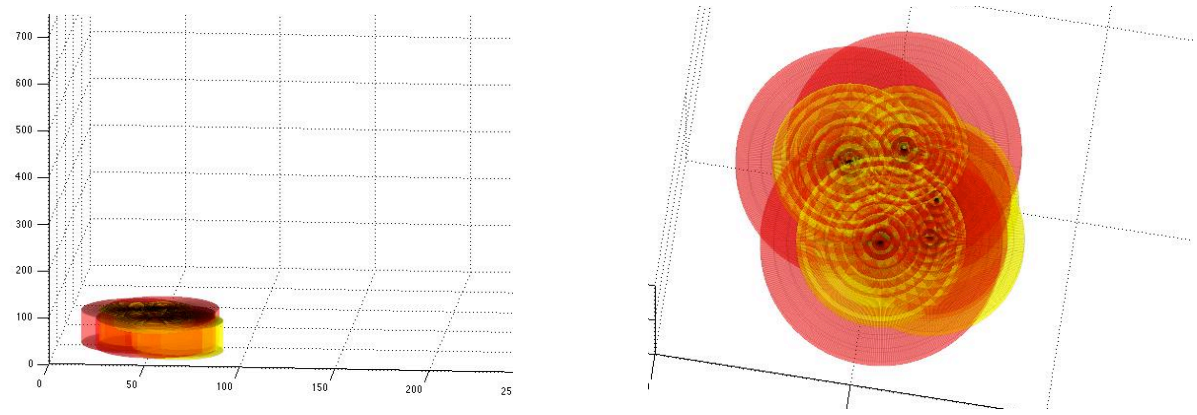


Figure 20. A cylindrical approximation of five neurons plotted over a 2500 µm x 2500 µm area viewed from an angle (left) and from the top (right)

In figure 20 we can see that if a large number of cells are plotted within a smaller volume, we get extensive overlap of axons, dendrites, and somas. If we visualize the same neurons in a larger volume we see no overlap, as displayed in Figure 17, we see no overlap.

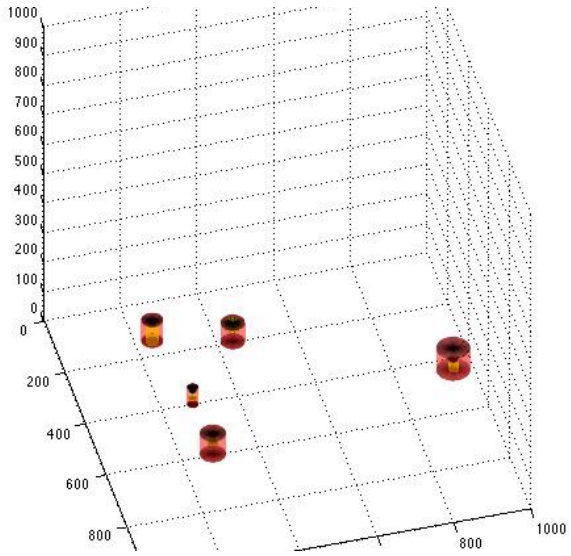


Figure 21. A cylindrical approximation of five neurons plotted over a 12500 µm x 12500 µm area

As we plot more and more neurons over a smaller volume we become less able to distinguish the overlap.

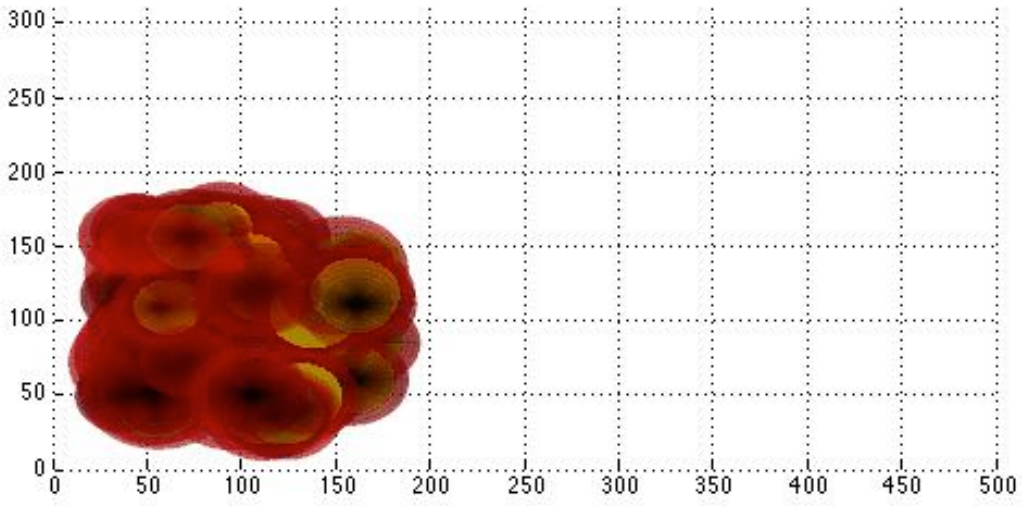


Figure 22. A cylindrical approximation of 100 neurons plotted over a 5000 μm x 5000 μm area (top view)

As mentioned above, the cylindrical approximation acted a more realistic model for the neuronal phenotypes than the boxes, but it made it more difficult for us to determine where the volume projections overlapped. We determined that where as well as how much volume the cells shared was important as the density of the branches varied throughout these volumes. In order to determine the coordinates of overlap with respect to the center vertical axis of each neuron we would have had to write code that solved for a very complex integral for the overlap of each neuron. The time it would take for Matlab to determine this value would have been too long to solve using the available Matlab built-in functions. Instead we determined that it would be enough to determine where the heights of neurons overlapped as well as radial overlap. We would then determine the probable density of branches at each point within these bounds. Given that the density probability was above a certain threshold that was later empirically derived for both neurons at the given coordinate a synapse would be recorded there. We then needed to derive probability density functions that accepted a radius and height as input for each neuronal phenotype.

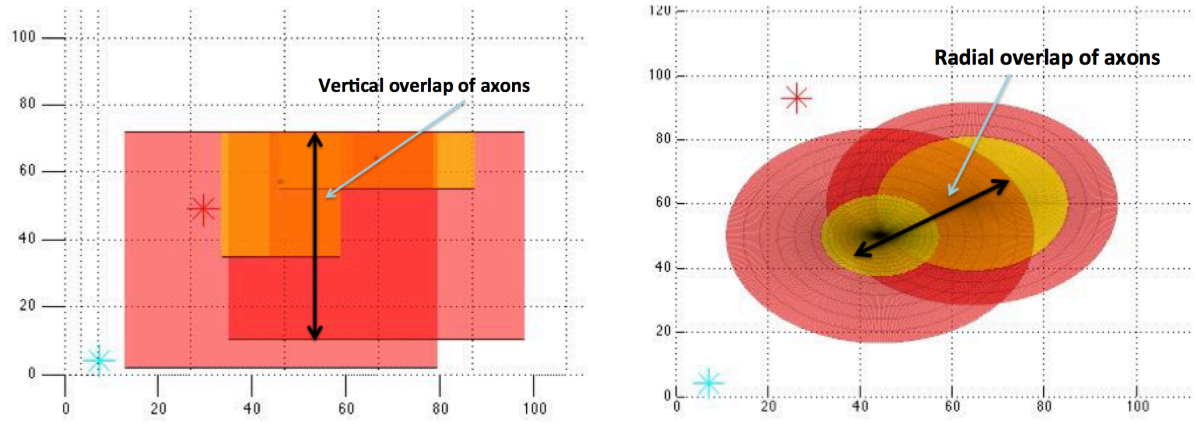


Figure 23. A visualization of the bounds for branch volume overlap between two neurons form the side (left) and top(right). The red star is a local microglial cell and the blue is peripheral microglial precursor

Axons can form synapses on the soma, dendritic branches, and axonal branches of other neuron so we considered the overlap of one neuron's axonal volume on another neurons soma, dendrites and axons. We were also concerned with the placement of terminals, because neurons are capable of releasing material into the extracellular environment as well as through synapses.

## 4.3 Derivation of Axonal and Dendritic Branch Densities

We wrote four main functions in order to determine the density probability equations for each phenotype. We first needed to create code that created and recorded the axonal and dendritic branches for each neuronal type. In one script called 'neuron_generator' we saved a set of parameter ranges derived from literature for each phenotype and use these to describe the branching behavior of the neurons.

| Phenotype |
| --- |
| Axon Radius |
| Apical Branch Frequency |
| Basal Branch Frequency |
| Axonal Branch Frequency |
| Average Branch Length |
| Nuclear Depth |
| Apical Tree Length |
| Number Of Primary Oblique Branches |
| Number Of Primary Apical Tuft Branches |
| Number Of Primary Dendritic Branches |
| Apical Branch Path Length |
| Basal Branch Path Length |
| Total Axon Branch Length |
| Branch Length Decay Rate |

Table 1. Parameters used to define each phenotype in the 'neuron_generator' function

These values were fed into a function called 'generator' written in a separate script that actually generates the branches at heights and radii designated in the initial parameters. We used a series of nested for loops to determine the branches of apical and basal dendrites and axonal branches. In each loop, a matrix containing the lengths, cylindrical coordinates of each primary branch and a radius ranging from a non-zero length and length of the branch was iterated over to generate a new branch point. The radius assigned to each branch corresponds to a 'sphere of possibility'. The branches of neurons are flexible and dynamic and need to be modeled as such. By associating a single branch with sphere a semi-randomly determined radius the branch can be said to exist in any conformation within that sphere. The sphere can never be so small that its volume is less than the volume of the branch. Within the for loop the code selects a random point within the primary branch's 'sphere of possibility' and generates two new branches originating at that location. New branches are also associated with a radius for its 'sphere of possibility' and become the primary branches for the next iteration. The branch length for neurons tends to drop

off as a function of order. The code continues to run the for loop the new branches as assigned a smaller and smaller length until all new assigned branches have a length less than its given branch frequency. The 'generator' function returns four matrices for apical, basal, and axonal branches and terminals. Each matrix contains the branch length, coordinate of the branch origin, and radius of the 'sphere of possibility'. The radius and length can then be used to determine the density of branching about that coordinate.

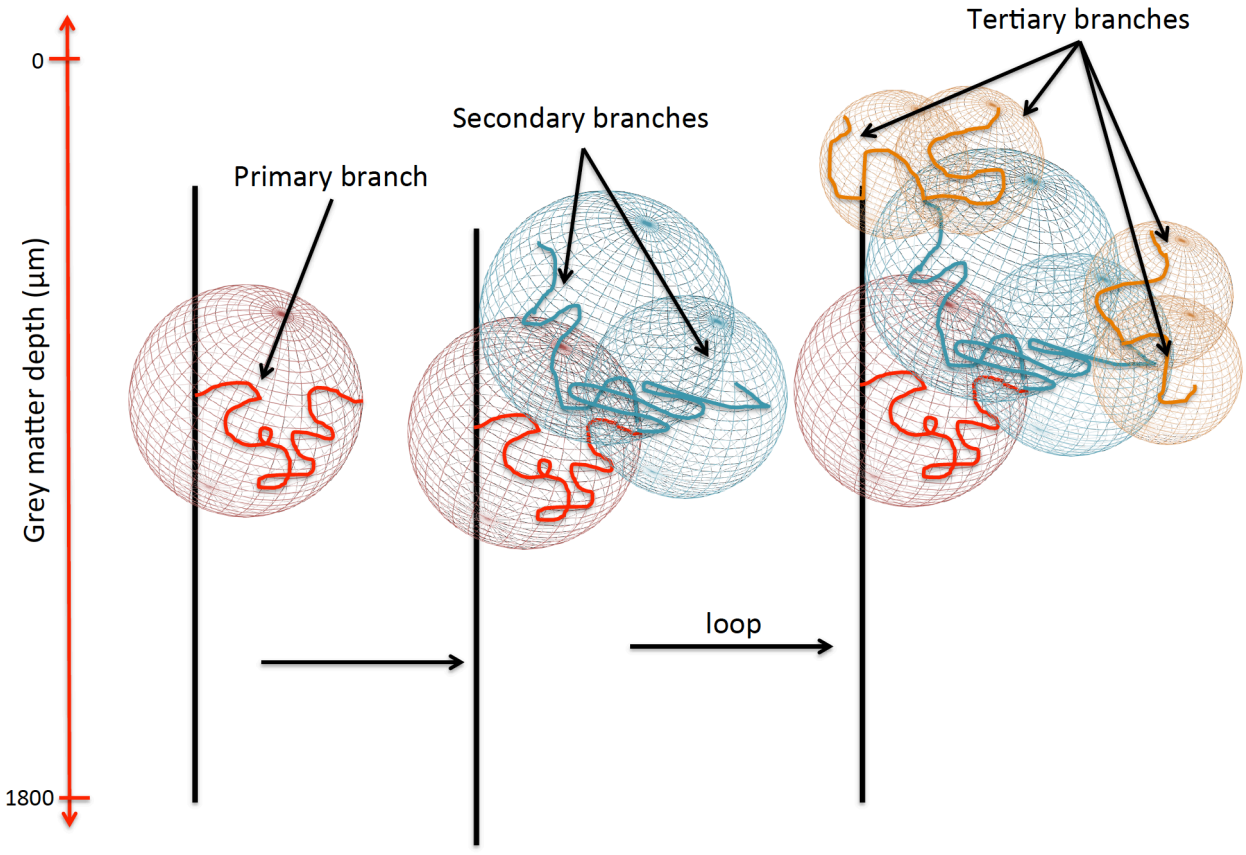


Figure 24. A visual schematic of the 'generator' function

We used the following functions in order to determine the density of branches associated with each point. *rad* is the radius for the 'sphere of possibility'. The approximate radius of a dendritic branch is 0.45 μm and the approximate radius of an axonal branch is 0.15 μm.

$$\rho_{dendritic} = 0.45^2\pi\frac{(length_{branch})}{\frac{4}{3}(rad)\pi} \quad (6)$$

$$\rho_{axonal} = 0.15^2\pi\frac{(length_{branch})}{\frac{4}{3}(rad)\pi} \quad (7)$$

The following are the results of the 'generator function'. From the plots we determined the number of branch points decreased as a function of radius. We also saw clustering of branch points about the approximate depth of the soma which was to be expected.

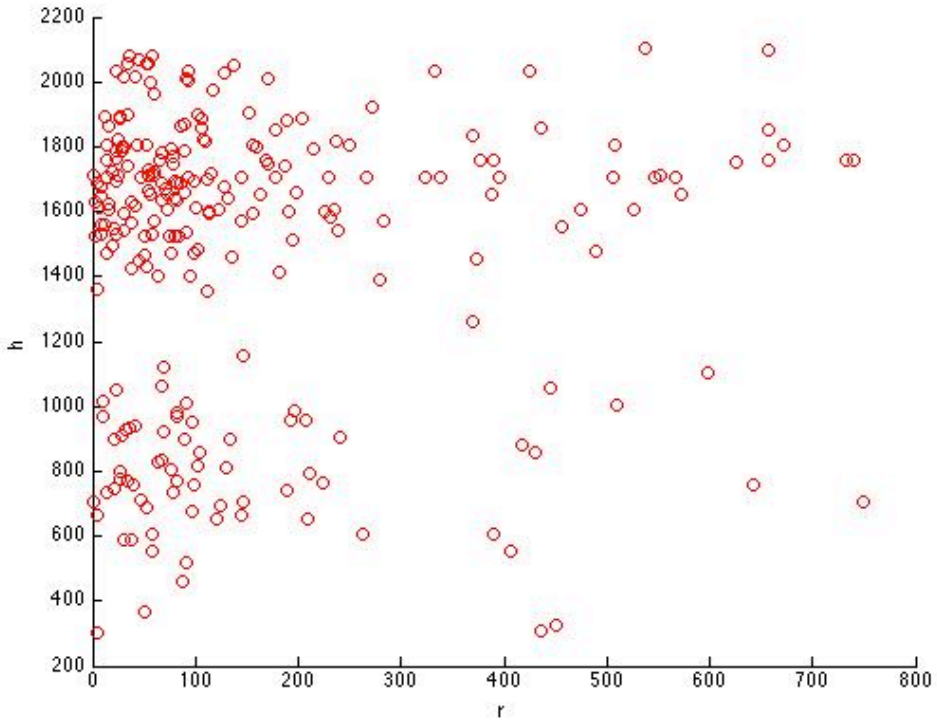


Figure 25. A plot of each axonal branch at their given (r, h) for an L2py neuron

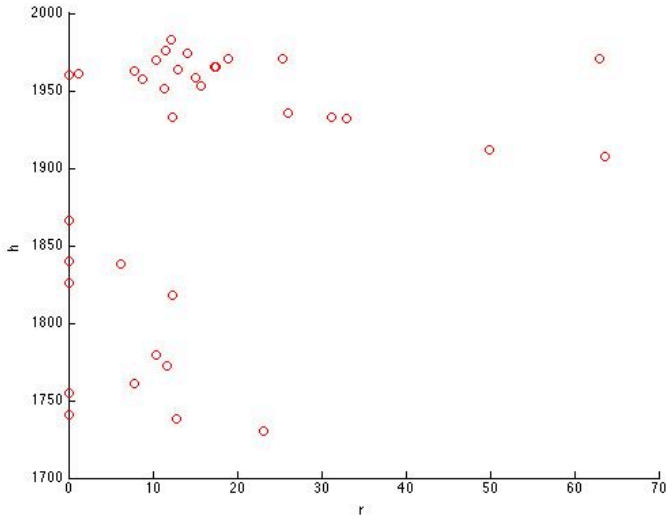


Figure 26. A plot of each dendritic branch at their given (r, h) for an L2py neuron

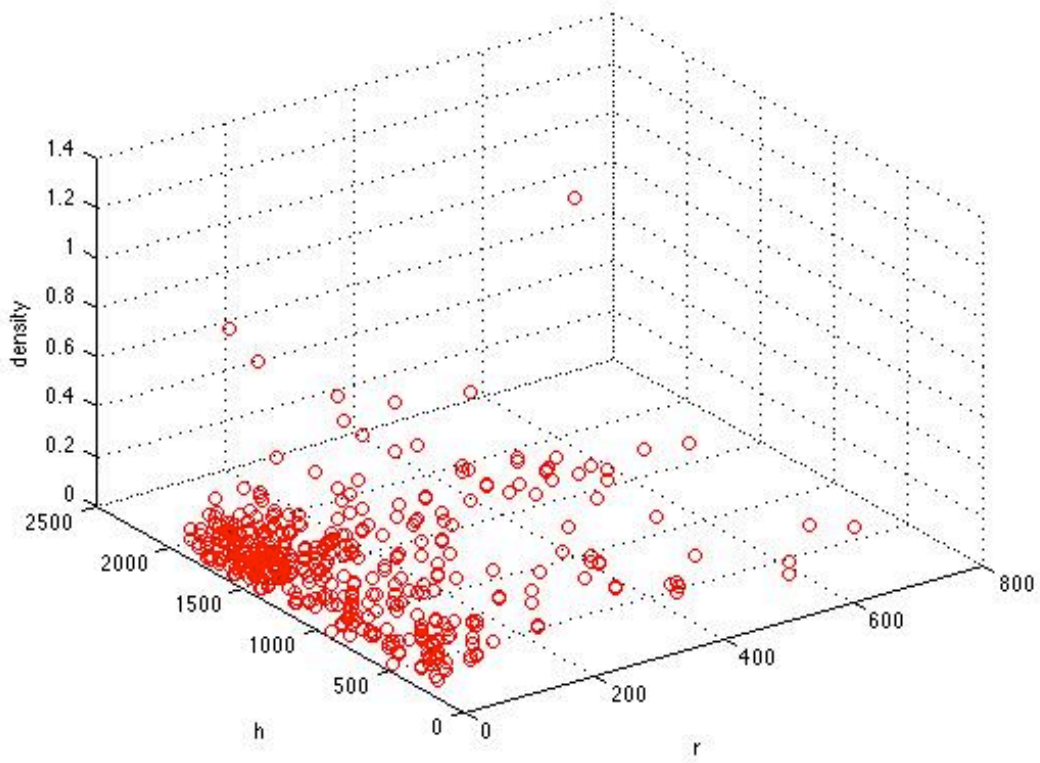


Figure 27. A multivariate scatter plot of each axonal branch density as a function of (r, h) of an L2py neuron

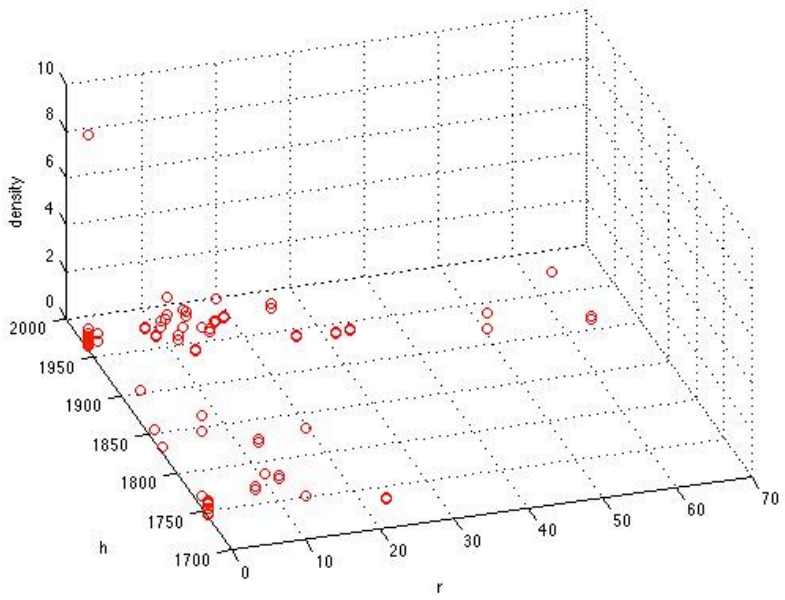


Figure 28. A multivariate scatter plot of each dendritic branch density as a function of (r, h) of an L2py neuron

## 4.4 Derivation of Density Probability Equation

Every time we ran the neuron generator it created a completely unique cell. In order to increase the reliability of our results we ran the generator a thousand times, created 1000 neurons and averaged the values associated with the 20 branches having the highest densities. These 20 densities and their corresponding coordinates were then used to derive the probability density function of each neuronal phenotype.

We needed to fit the top 20 densities with a model equation in order to first derive a density equation for the given phenotype. Due to the irregular and non-linear behavior of neuronal branching we were unable to perform a linear, exponential, or any Matlab or Excel built-in fit model on the averaged points. We decided to use a three-dimensional averaged Gaussian function to fit the results. Each of the 20 points became a Gaussian function weighted

by a proportionality constant derived from its density. Those individual Gaussian functions were then averaged.

Here is the general equation for the Gaussian fit:

$$\rho(r,h) = \frac{1}{20}\sum_{n=1}^{20} w_n \frac{1}{2\pi\sigma} e^{-\frac{(r-\mu_{r,n})^2+(h-\mu_{h,n})^2}{2\sigma^2}} \quad (8)$$

$$w \propto \rho, \;\; \sigma = constant$$
$$\mu_{r,n} = r_{model\ density}$$
$$\mu_{h,n} = h_{model\ density}$$

We plotted these density functions in order to show their resemblance to branch volume projections derived from one literature source.

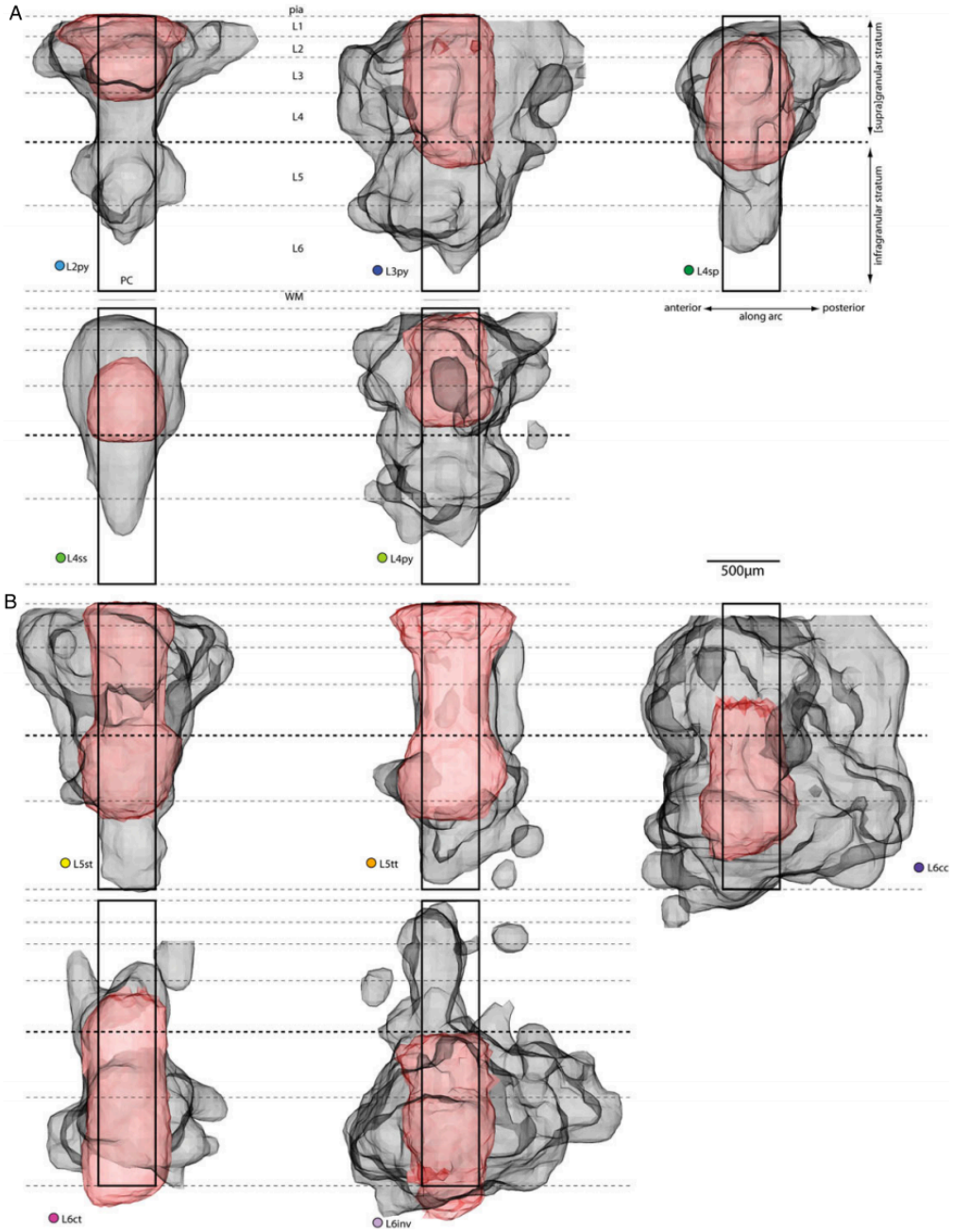


Figure 29. An image of the dendritic branch volume projections (red) and axonal branch volumes (black) taken from a paper published by Narayanan et al, 2015.

L2py

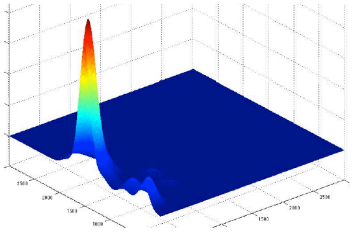

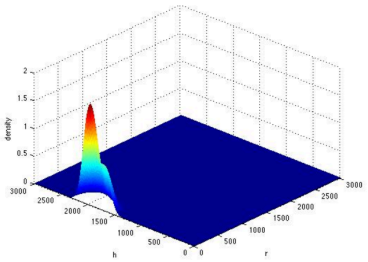


L3py

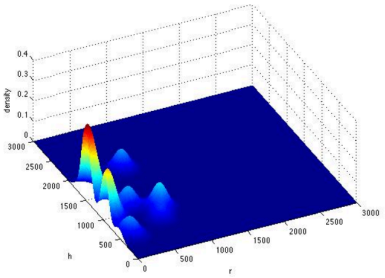


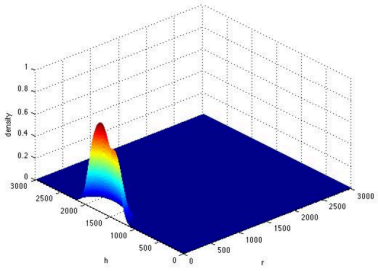


L4sp

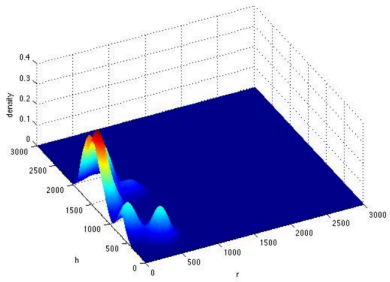


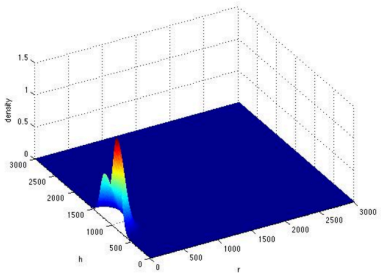


L4ss

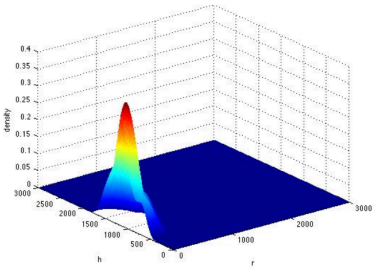


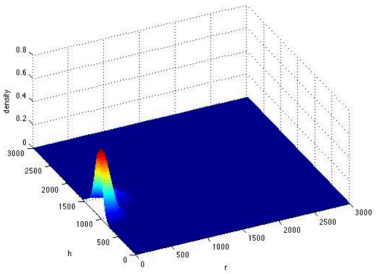


L4py

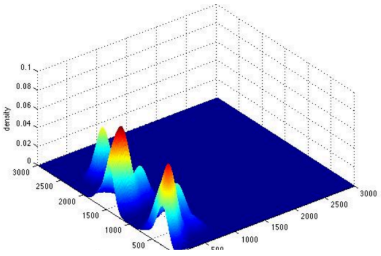


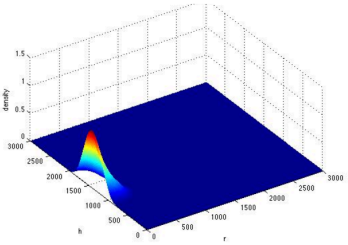


L5st

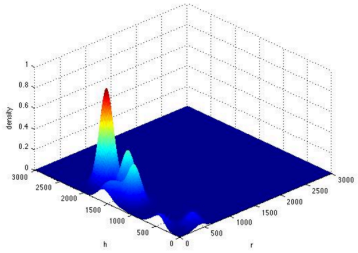


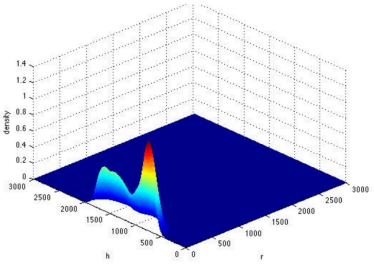

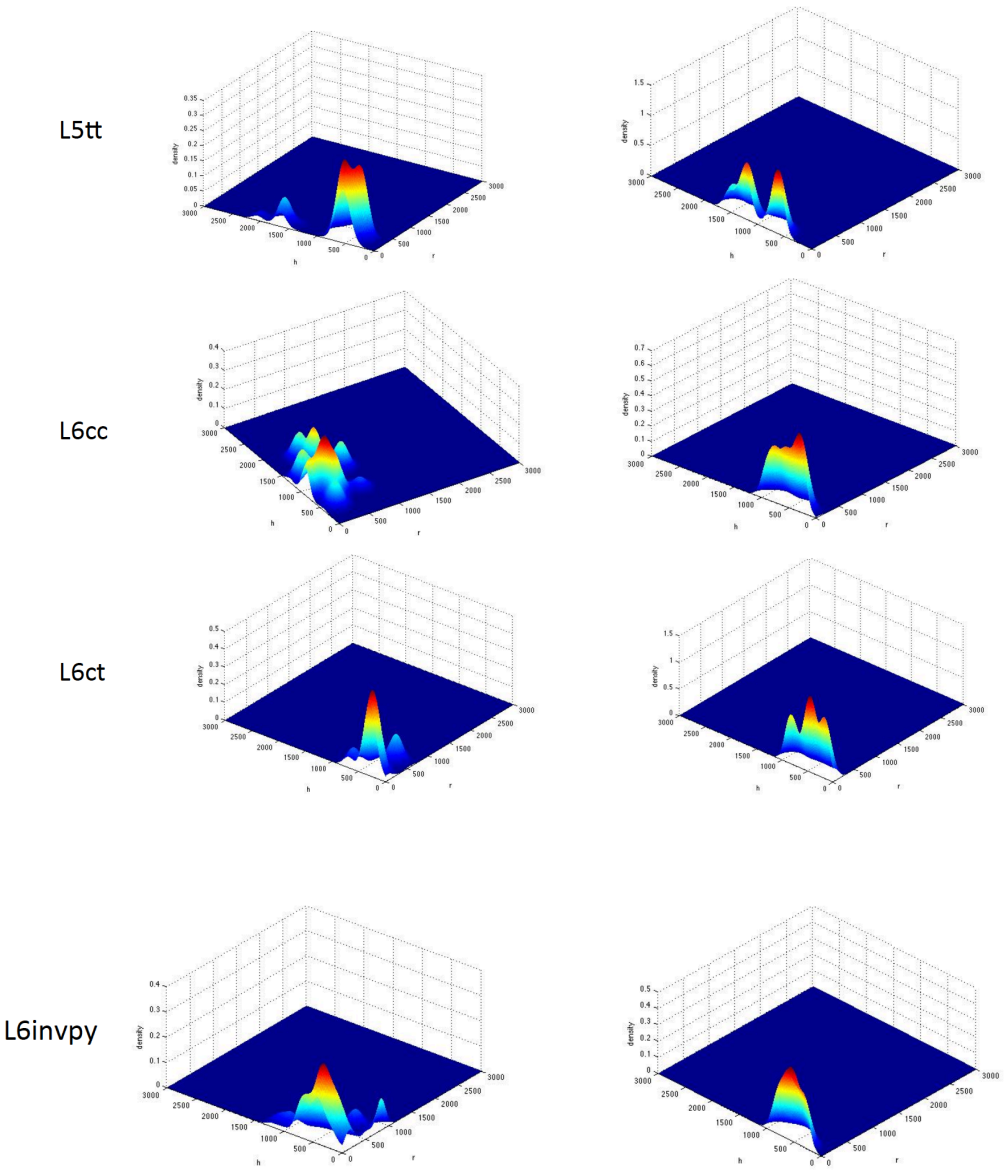


Figure 30. The graphs of density functions determined for each phenotype's axons (left) and dendrites (right)

The final step was to use the density equations to derive the probability density equations. By dividing the density function by the total density, taking the $\log_{10}$ of that value and dividing it all by -10, we obtained out density functions.

$$P(r,h) = \frac{-10}{\log_{10}\frac{\rho(r,h)}{D}} \quad (9)$$

$$D = \int_0^{2\pi}\int_0^{\infty}\int_0^{2000} \rho(r,h)\, r\, dh\, dr\, d\theta \quad (10)$$

We were able to use this equation to check the probability density of each point within overlap boundaries for each paired neuron. We had to first convert every investigated coordinate into a cylindrical coordinate with respect to each neuron's point of origin (the center of the soma). We could then input the coordinate in terms of *r* and *h* into the probability density equation for the correct phenotype. The function returns three outputs, the axonal probability, the dendritic probability and a two-dimensional matrix containing coordinates to axonal terminals derived from the original 'generator' function. For branch overlap we determined that the threshold for synaptic formation of 0.95 for both neuronal probabilities. This gave a number of synapses derived from previously performed live experiments. For terminal overlap, we needed only to check the density probability of the potential post-synaptic neuron. We determined that a threshold probability of 0.80 generally allowed the majority of axon terminals to form synapses. We didn't design a probability density equation for somas as we considered them to be the only rigidly situated body in the entire model. We selected points only at the radius of the soma if they were within the overlap range we checked if a terminal ended at the same point, as well as the axonal density probability of the presynaptic neuron. If a terminal was a match, we recorded a synapse there or if the axon probability was above 0.9. We recorded the coordinates of

synapses in a two-dimension matrix for each neuron. The height of the matrix was equivalent to the number of neurons one neuron had overlap with.

# Part 5: Combining the Kinetic Equations with the Spatial Representation

## 5.1 Methodology

In order to incorporate the cylindrical spatial representation with the pseudo-spatial model, we needed to write code that applied and updated coordinates associated with certain variables such as $PrP^{Sc}$ during the same for loop used to iterate over the ODE solver. We realized that the massive amount of data that would need to be stored was too great to be recorded in the same three-dimensional matrix containing the dependent variable concentrations, thus we adopted a similar solution and wrote a separate three-dimensional matrix containing all of the spatial data. The data could then be updated and imputed as variables in the kinetic equations within the same loop.

Similar to the pseudo-spatial matrices, the length of the third dimension of the neuronal matrix was equivalent to the number of neurons and the length of the microglial matrix was equivalent to the number of microglia. Each cell therefore had a two-dimensional matrix containing its associated values. The variables considered within this matrix include the same variables summed and updated outside of the ode solver during each loop iteration. Unlike in the pseudo-spatial model the new model had concrete information about the distance between neurons as well as the locations of synapses. We could then use this spatial information to determine the time needed for soluble signaling molecules to reach their destination and gave a better approximation of the amount of signaling molecules received by each neurons based on that distance traveled. We had the opportunity to also incorporate diffusion equations to give the best approximation of molecular distribution, but lacked the mathematical expertise to do so. Instead we assumed that molecules travel with a constant velocity inversely proportional to their mass to potential targets. We realized that in order to keep track of a continuous release of

soluble molecules we would need to record a coordinate associated with a released concentration at each time step as well as update its progress during each iteration. Not only would keeping track of so many variables overwhelm the capacity of the matrix but add a large amount of time to complete the simulation. Instead we rewrote the differential equation functions so that 'waves' of signals were generated at certain time intervals, which allowed us to the then track these 'waves' of signals in the spatial matrix. As these 'waves' approach a radius of equivalent distance from their point of origin to a neurons. The waves concentration is then adjusted according to how much was bound to the neuron's receptors.

When a wave reaches the coordinate of a microglia cell we similar adjust the amount based on how mush was received by the cell. Because we also know the identity of the neuron that produced each wave of signals, we can identify which neurons the activated microglial cell will migrate toward. The larger the amount of molecules received by the microglial cell the stronger the pull of the distress signal and we could then set the microglia on a linear path toward that neuron. The path however is not absolute upon activation, but the microglia can change its trajectory based on the strengths of the signals it receives. That way it will always move in the direction of the most damage. The distance between microglia and neurons is adjusted each time until the distance is close enough that phagocytosis can occur.

Exosomes containing $PrP^{Sc}$ are less numerous than soluble molecules and were able to track them individually within the matrix. Because we did not have to treat them as waves we were able to approximate their movement using Brownian motion. The location of each exosome was allowed to move 10 μm/s in any direction. If it came within the bounds of another neuron's axonal or dendritic radius we calculated the corresponding probability density at that location. If

the probability was higher that 0.90 the said then said that the exosome could be endocytosed or fused with the membrane of that neuron.

With the concrete spatial information we were able make a better approximation to PrP protein trafficking. Synaptic firing is a frequent and important event to regular $PrP^{C}$ trafficking. As molecules such as copper are released during a firing even it the synapse, $PrP^{C}$ can bind some of that copper, which then triggers endocytosis, followed by release of $Cu^{2+}$ with the cell and recycling of $PrP^{C}$. As mentioned earlier, this regular cycling may play an essential role in $PrP^{Sc}$ propagation and invasion of the neuron's endosome system. We assigned an initial firing time to each neuron based on its distance from the initially infected cell. Upon a firing event occurring at consistent intervals following the initial firing, concentrations of key molecules, such as copper are released into the synapse, we then adjust the concentration of copper available for binding as well that lost by the pre-synaptic neurons. We chose not to extend this system beyond copper as it is involved with PrP protein and therefore necessary to track spatially. Within the spatial matrix we assigned concentrations of $PrP^{C}$ to every synapse and terminal, so we were then able to track the specific localizations of PrP protein. We also populated the matrix with a number of MVBs at randomly assigned coordinated in dendrites, axons, and somas. PrP protein and binding partners could then be trafficked to the closest MVB location with its same branch type or soma body. Populations of PrP protein localized to the same MVB concatenated their values to one population. PrP localized within MVBs could then be targeted to recycling endosomes, endolysosomes, retrograde transport vesicles or exosomes. Each of these localizations also has an associated coordinates. Populations of PrP protein trafficked to the golgi system, ER, and cytosol are not associated with coordinates but treated just as general differential equations. By knowing the specific locations of $PrP^{C}$ and $PrP^{Sc}$ we can apply prion conversion rates to specific

localizations of protein to get a better approximation of the proliferation mechanism. We explored the possibility that particularly high concentrations of $PrP^{Sc}$ with synapses can infect the receiving neuron, though have yet to find concrete evidence within the literature that this occurs.

All of these variables and their associated locations are organized in the matrix in Table 2. We consider the number of entries initially used to populate the matrix is concrete.

| | | | | | | repeated for each entry |
|---|---|---|---|---|---|---|
| synapses formed with neuron of index n | PrPSc | PrPC | x | y | z | . . . |
| same for number of nuerons in overlap, n | . . . | . . . | . . . | . . . | . . . | . . . |
| PrP associated with early endosomes | PrPSc | PrPC | x | y | z | . . . |
| PrP associated with MVBs | PrPSc | PrPC | x | y | z | . . . |
| PrP associated with recyling endosomes | PrPSc | PrPC | x | y | z | . . . |
| PrP associated with retrograde transport | PrPSc | 0 | x | y | z | . . . |
| PrP associated with endolysosomes | PrPSc | PrPC | x | y | z | . . . |
| PrP associated with exosomes | PrPSc | 0 | x | y | z | . . . |
| microglial distance | microglial index, m | distance | . . . | | | |
| distress sinalling molecule 'waves' | [signal] | distance from origin | . . . | | | |

Table 2. Organization of the matrix containing tracked variables.

A similar matrix was defined for microglial cells, but it only contained the coordinates of released signaling waves.

# Discussion

We were been able to write all of our desired differential equations into Matlab and obtained results for different sized neuronal ensembles. Our classical, pseudo-spatial model revealed interesting stepwise patterns in variable concentrations that we believe were caused by the protein trafficking behavior we included. We are currently working on statistical analysis to determine how well our model approximated neuronal morphologies.

Without the kinetic results from the superimposed spatial model, we are currently unable to determine the influence of our spatial approximations on the behaviors of molecules during our simulation of the disease. We expect to see similar trends in the behavior of the model and we would also gain more detailed account of those trends. By manipulating the model we can alter the disease so that we only see the effects of one or two factors at a time such as infection without exosomal release or suppression of certain genes. We would be able to determine important rates and rate modifiers including a rate of cellular cross-infection, the effects of cell density on the rate of the disease, and which transfer mechanism was most effective.

Under the assumption that the model produces significantly different results, we plan to create a more user-friendly environment so that sets of rate equations can be imputed for any neurondegerative disease. Again, prion disease is one of many aggregate-based conditions and therefore may behave in a similar fashion when observed using a spatial approximation. Other future plans for the model include incorporation of diffusion equations to more accurately relay molecular distributions. We also plan to return to our model two and attempt to create a model system with other cell types including astrocytes and oligodendrocytes which also contribute significantly to cellular response to infection.

# Conclusion

By making a set of general approximations we were able to generate a spatial representation of a small neural ensemble within the human neocortex. Though we were not able to determine how such a model affects the results of superimposed kinetic equations, we were able to complete a model that generates realistic neuronal branch overlap or crowding, branch densities, phenotypic diversity, movement of molecules, and exchange of molecules as well a functioning set of classic kinetic equations.

We have yet to determine a better approximation than cylinders to reflect the radial symmetry of neurons, but would likely improve our model by including non-vertical cylindrical approximations, meaning the cylinder have off-set vertical axii. We also want to expand the number of phenotypes included in the ensemble, which may have morphologies that require a different approximated simple geometry. We realize that the radial-symmetry on which we base our approximations is a very broad assumption as branching morphologies are unique and often do not have a clear symmetry. Our model would benefit from more diversity in neuronal subtypes.

The recent renaissance of biomathematics has provided new opportunities to lend computational analysis to biological systems analysis. Models study more than what a single conventional biochemical lab can at once, but these models cannot exist without the collective scientific foundation produced through experimental work. Computational analysis relies on the work accomplished by traditional labs in order to have material with which to build models. Modeling systems can make experimental work more efficient by predicting any number of potential outcomes, so as to minimize the need for expensive trial and error. Modeling works where other techniques may fall short by predicting the behavior of molecules that cannot be

readily observed. Models can be as detailed or as simple as is necessary to describe the system. One would assume that the higher the level the detail the better, but as we have demonstrated, simplifications such as our first-order approximations can make studying general trends in the data easier. We successfully generated a model system by representing neurons as cylinders. This approximation allowed us to determine the overlap between branches, but we relied on additional information, the density probabilities, in order to increase the accuracy of our model. We created a model that contains both simplifications and more complex components, so that it is not only a reliable representation of the human brain, but also an accessible and malleable environment with which to study disease.

# Acknowledgements

The research used to develop this thesis was in part funded by the Howard Hughes Medical Institute, Undergraduate Biological Sciences Education Program, The College of William and Mary, and The Roy R. Charles Center for Academic Excellence at The College of William and Mary.

## Sources

Sources not specifically cited with the text were used to identify variables in the model


Aguzzi, A. and Falsig., J. Prion propagation, toxicity and degradation. *Nature Neuroscience*. **2012**. 15(7). 936-939.

Akhter, R., Sanphui, P., & Biswas S. C. The essential role of p53-up-regulator of apoptosis (PUMA) and its regulation by FoxO3a transcription factor in β-amyloid-induced neuron death. *The Journal of Biological Chemistry.* **2014**, 298, 10812-10822.

Ambros-Ingerson, J. and Holmes, W.R. Analysis and comparison of morphological reconstructions of hippocampal field CA1 pyramidal cells. *Hippocampus.* **2005**; 15:302-315.

Amor, S., Peferoen, L. A. N., Vogel, D. Y. S., Breur, M., van der Valk, P., Baker, D., *et al.* Inflammation in neurodegenerative diseases – an update. *Immunology, The Journal of Cells, Molecules, Systems, and Technologies.* **2013***,* 141**,** 151-166.

Asuni, A. A., Gray, B., Bailey, J., Skipp, P., Perry, V. H., & O'Connor, V. Analysis of the hippocampal proteome in ME7 prion disease reveals a predominant astrocytic signature and highlights the brain-restricted production of clusterin in chronic neurodegeneration. *The Journal of Biological Chemistry.* **2014***,* 289, 4532-4545.

Asuni, A. A., Gray, B., Bailey, J., Skipp, P., Perry, V. H., & O'Connor, V. Analysis of the hippocampal proteome in ME7 prion disease reveals a predominant astrocytic signature and highlights the brain-restricted production of clusterin in chronic neurodegeneration. *The Journal of Biological Chemistry.* **2014***,* 289, 4532-4545.

Basova, L.V., Kurnikov, I.V., Wang, L., Ritov, V.B., Belikova, N.A., Vlasova, I.I., Pacheco, A.A., et al. Cardiolipin switch in mitochondria: shutting off the reduction of cytochrome *c* and turning on peroxidase activity. *Biochemistry*. 46(11); 3423-3434; **2007**.

Benavides-Piccione, R., Hamzaei-Sichani, F., Ballesteros- Yáñez, I., DeFelipe, J., and Yuste, R. Dendritic size of pyramidal neurons differs among mouse cortical regions. *Cerebral Cortex*. **2005;** 16; 990-1001.

Biasini, E., Unterberger, U., Solomon, I. H., Massignan, T., Senatore, A., Bian, H., *et al*. A mutant prion protein sensitizes neurons to glutamate-induced excitotoxictiy. *J Neurosci*. **2013**, 33, 2408-2418.

Biber, K., Neumann, H., Inoue, K., & Boddeke, H. W. G. M. Neuronal 'on' and 'off' signals control microglia. *TRENDS in Neurosciences.* **2007**, 30, 596-602;.

Biber, K., Neumann, H., Inoue, K., & Boddeke, H. W. G. M. Neuronal 'on' and 'off' signals control microglia. *TRENDS in Neurosciences.* **2007**, 30, 596-602.

Block, M.L, and Hong, J. Microglia and inflammation-mediated neurodegeneration: multiple triggers with common mechanism. *Progress in Neurobiology*. 76; 71-98; **2005**.

Boland, B., Kumar, A., Lee, S., Platt, F.M., Wegiel, J., Yu, W.H., and Nixon, R. Auotphagy induction and autophagosome clearance in neurons: relationship to autophagic pathology in Alzheimer;s disease. *The Journal of Neuroscience*. **2008;**28(27); 6926-6937.

Botto, L., Cunati, D., Coco, S., Sesana, S., Bulbarelli, S., Biasini, E., *et al*. Role of lipid rafts and GM1 in the segregation and processing of prion protein. *PLoS ONE*. **2014**, 9, 1-14.

Bush, A. I. Metals and neuroscience. *Current Opinion in Chemical Biology*. **2000**, 4, 184-191.

Campana V., Sarnataro, D., and Zurzolo, C. The highways and byways of prion protein trafficking. *TRENDS in Cell Biology*. **2005**, 15, 102-111.

Carreras, M., C. and Poderoso, J., J. Mitochondrial oxide in the signaling of the integrated responses. American Journal of Cell Physiology. **2007**, 1569-1580, 292(5).

Cho, I. S., Spinner, D. S., Kascaak, R. J., Meeker, H. C., Kim, B. S., Park, S. Y. et al. Altered lymphocyte proliferation and innate immune function in scrapie 139A- and ME7-infected mice. *Viral Immunolgy*. **2013**, 26, 192-200.

Eddelstein-Keshet, L. Mathematical Models in Biology. New York, NY. 2005.print.

Eichhoff, G., Brawek, B., and Garaschuk, O. Microglial calcium signal acts as a rapid sensor of single neuron damage *in vivo. Biochimica et Biophysica Acta – Molecular Cell Research*. 1813(5); 1014-1024; **2011**.

Färber, Katrin and Kettenmann, H. Physiology of microglial cells. *Brain Research Reviews*. 48; 133-143; **2005**.

Finkel, T. Signal transduction by reactive oxygen species. *The Journal of Cell Biology.* **2014**, 194, 7-15.

Fleury, C., Mignotte, B., Vayssière, J. Mitochondrial reactive oxygen species in cell death signaling. *Biochimie*. 84(2,3); 131-141. **2002**.

Fournier, J. Cellular prion protein electron microscopy: attempts/limits and clues to synaptic trait. Implications in neurodegeneration process. **2008.** *Cell Tissue Res*. 332; 1-11.

Ghaemmaghami, S., Phuan, P., Perkins, B., Ullman, J., May, B.C.H., Cohen, F.E., et al. Cell division modulates prion accumulation in cultured cells. *PNAS*. **2007;**104(46); 17971-17976.

Gilch, S., Bach, C., Lutzny, G., Vorberg, I., Schätzl, H.M. Inhibiton of cholesterol recycling impairs cellular $PrP^{Sc}$ propagation. *Cellular and Molecular Life Sciences*. 66; 3979-3991. **2009**.

Gittins, R. and Harrison, P.J. Neuronal density, size and shape in the human anterior cingulate cortex: a comparison of Nissl and NeuN staining. *Brain Research Bulletin*. 63; 155-160; **2004**.

Goold, R., McKinnon, C., and Tabrizi, S.J. Prion degradation pathways: potential for therapeutic intervention. *Molecular and Cellular Neuroscience*. 66; 12-20; **2015**.

Greer, M.L., Pujo-Menjouet, L., and Webb, G.F. A mathematical analysis of the dynamics of prion proliferation. *The Journal of Theoretical Biology*. 242; 598-606; **2006**.

Haigh, C. L., McGlade, A. R., Lewis, V., Masters, C. L., Lawson, V. A., & Collins, S. J. Acute exposure to prion infection induces transient oxidative stress progressing to be cumulatively deleterious with chronic propagation in vitro. *Free Radical Biology and Medicine*. **2011**, 51, 594-608.

Hartmann, C. A., Martins, V. R., & Lima, F. R. S. High levels of cellular prion protein improve astrocyte development. *Federation of European Biochemical Societies Letters*. **2013**, 587, 238-244.

Herculano-Houzel, S. The glia/neuron ratio: how it varies uniformly across brain structures and species and what that mean for brain physiology and evolution. *GLIA*. 62(9); 1377-1391; **2014**.

Herculano-Houzel, S. The human brain in numbers: a linearly scaled-up primate brain. *Frontiers in Human Neuroscience*. 2(31); 1-11; **2009**.

Hetz, C. and Mollereau, B. Disturbance of endoplasmic reticulum proteostasis in neurodegenerative disease. *Nature Reviews: Neuroscience*. 15; 233-249; **2014**.

Homma, T,, Ishibashi, D., Nakagaki, T., Satah, K., Sano, K., Atarashi, R., & Nishida, N. Increased expression of p662/SQSTM1 in prion disease and its association with pathogenic prion protein. *Scientific Reports*. **2014**, 4, 1-7.

Hori, Y. S., Kuno, A., Hosoda, R., & Horio, Y. Regulation of FOXOs and p53 by SIRT1 modulators under oxidative stress. *PLoS One*. **2013**, 8, 1-8.

Huang, H., and Tindall, D. J. Dynamic FoxO transcription factors. *Journal of Cell Science*. **2007**, 120, 2479-2487.

Hughes, M.M., Field, R.H., Perry, V.H., Murray, C.L., and Cunningham, C. Microglia in the degenerating brain are capable of phagocytosis of beads and of apoptotic cells, but do not efficiently remove PrPSc, even upon LPS stimulation. *GLIA*. 58; 2017-2040; **2010**.

Jacobs, K.M., Bhave, S.R., Ferraro, D.J., Jaboin, J.J., Hallahan, D.E., and Thotal, D. GSK-3beta: A bifuntional role in cell death pathways. *International Journal of Biology.* 2012; 1-11; **2012**.

Jalland, C. M. O., Benestad, S. L., Ersdal, C., Scheffler, K., Suganthan, R., Nakabeppu, Y., *et al.* Accelerated clinical course of prion disease in mice compromised in repair of oxidative DNA damage. *Free Radical Biology and Medicine.* **2014**, 1-7, 68.

Jeon, J., Park, B., Jung, J., Jang, Y., Shin, E., & Park, Y. W. The soluble form of the cellular prion protein enhances phagocytic activity and cytokine production by human monocytes via activation of ERK and NF- κB. *Immune Network*. **2013**, 13, 148-156.

Jurgens, H. A., & Johnson, R. W. Dysregulated neuronal-microglial cross-talk during aging, stress and inflammation. *Exp Neurol.* **2012,** 40-48, 233(1).

Kozlowski, H., Janicka-Klos, A., Brasun, J., Gaggelli, E., Valensin, D., and Vensin, G., Copper, iron, and zinc ion homestasis and their role in neurodegenerative disorders, (metal uptake transport. distribution, and regulation). *Coordination Chemistry Reviews*. **2009**, 253, 2665-2685.

Lainé, J., Marc, M., Sy, M., and Axelrad, H. Cellular and subcellular morphological localization of normal prion protein in rodent cerebellum. *European Journal of Neuroscience.* 14; 47-56; **2001**.

Larkman, A. and Mason, A. Correlations between morphology and electophysiology of pyramidal neurons in slices of rat visual cortex. I. establishment of cell classes. *The Journal of Neuorscience.* **1990;** 10(5); 1407-1414.

Li, J., Lee, B., and Lee, A.S. Endoplasmic reticulum stress-induced apoptosis: multiple pathways and activation of p53-up-regulated modulator of apoptosis (PUMA) and NOXA by p53. *Journal of Biological Chemistry.* **2006**, 281, 7260-7270.

Li, J., Lee, B., and Lee, A.S. Endoplasmic reticulum stress-induced apoptosis: multiple pathways and activation of p53-up-regulated modulator of apoptosis (PUMA) and NOXA by p53. *Journal of Biological Chemistry.* **2006**, 281, 7260-7270.

Liley, D.T. and Wright, J.J. Intercortical connectivity of pyramidal and stellate cells: estimates of synaptic densities and coupling symmetry. *Network: Computation in Neural Systems*. **1994**; 5: 15-189.

Liley, D.T.J. and Wright, J.J. Intercortical connectivity of pyramidal and stellate cells: estimates of synaptic densities and coupling symmetry.

Lima, F. R. S., Arantes, C. P., Muras, A. G., Nomizo, R., Brentani, R. R., & Martins, V. R. Cellular prion protein expression in astrocytes modulated neuronal survival and differentiation. *Journal of Neurochemistry.* **2007**, 103, 2164-2176.

Linden, R., Martins, V.R., Prao, M.A.M., Cammarota, M., Izquierdo, I., and Brentani, R.R. Physiology of the prion protein. *Physiological Reviews*. 88(2); 673-728; **2008**.

Liu, B., Chen, Y., and St. Clair, D.K. ROS and p53: a versatile partnership. *Free Radical Biology and Medicine*. 44; 1529-1535; **2008**.

Liu, H., Nishitoshi, H., Ichijo, H., and Kyrikis, J.M. Activation of apoptosis signal-regulationg kinase 1 (ASK1) by tumor necrosis factor receptor-associated factor 2 requires prior dissociation of ASK1 inhibitor thioredoxin. *Molecular and Cellular Biology*. 20(6); 2198-2208; **2000**.

Liu, T., Yi, W., Feng, B., Zhou, Z., & Xiao, G. IGF-1-induced enhancement of *PRNP* expression on the negative regulation of transcription factor FOXO3a. *PLoS ONE.* **2013**, 8, 1-11.

Lübke, J., Markram, H., Frotscher, M., and Sakmann, B. Frequency and dendritic distribution of autapses established by layer 5 pyramidal neurons in the developing rat neocortex: comparison with synaptiv innervation of adjacent neurons of same class. *The Journal of Neuroscience*. 16(10); 3209-3218; **1996**.

Marzo, L., Maijanovic, Z., Browman, D., Chamoun, Z., Caputo, A., and Zurzolo, C. 4-hydorxytamoxifen leads to $PrP^{Sc}$ clearance by conveying both $PrP^{C}$ and $PrP^{Sc}$ to lysosomes independent of autophagy. *Journal of Cell Science*. **2013;**126:1345-1354.

Masel, J., Jansen, V.A.A., and Nowak, M.A. Quantifying the kinetic parameters of prion replication. *Biophysical Chemistry*. 77; 139-152; **1999**.

Medías, M., Eri, ZS., Freund, T.F., and Gulyás, A.I. Total number and distribution of inhibitory and excitatory synapses on hippocampal CA1 pyramidal cells. *Neuroscience*. 102(3); 527-540; **2001**.

Megías, M., Emri, T., Freund, F. and Gulyás, A.I. Total number of distribution of inhibitors and excitatory synapses on hippocampal CA1 pyramidal cells. *Neuroscience*. **2001**;102(3):527-540.

Michel, B., Meyerett-Reid, C., Johnson, T., Ferguson, A., Wyckoff, C., Pulford, B., *et al.* Incunabular immunological events in prion trafficking. *Scientific Reports.* **2**(440): 1-12; 2012.

Mingheti, l., Ajmone-Ct, M.A., De Berardinis, M.A., and De Simone, R. Microglial activation in chronic neurodegenerative disease: roles of apoptotic neurons and chronic stimulation. *Brain Research Reviews*. 48; 251-256; **2005**.

Mironov Jr., A., Latawiec, D., Willie, H., Bouzamondo-Bernstein, E., Legame, G., Williamson, R.A., et al. Cystolic prion protein in neurons. *The Journal of Neuroscience*. 23(18); 7183-7193; **2003**.

Mittelbronn, M., Dietz, K., Schluesener, H.J., Meyermann, R. Local distribution of microglia in the normal adult human central nervous system differs by up to one order of magnitude. *Acta Neuropathol*; 101; 249-255; **2001**.

models of prion disease. *Neuropathology and Applied Neurobiology*. 40; 311-326; **2014.**

Moishima, M. and Kawaguchi, Y. Recurrent connection patterns of corticostriatal pyramidal cells in frontal cortex. *The Journal of Neuroscience*. **2006**; 26(16):4394-4405.

Moore, R.A., Sturdevant, D.E., Cheesebro, B., and Priola, S.A. Proteonomics analysis of amyloid and nonamyloid prion disease phenotypes reveals both common and diveregent mechanisms of neuropathogenesis. *Journal of Proteome Research*. **2014**;13:4620-4634.

Moreira, M.E. and Marcinski, M.A. Apoptotic cell and phagocyte interplay: recognition and consequences in different cell systems. *Annals of the Brazilian Academy of Sciences*. **2004;**76(1): 93-115.

Mowla, S. N., Perkins, N. D., & Jat, P. S. Friend or foe: emerging role of nuclear factor kappa-light-chain-enhancer of activated B cells in cell senescence. *Onco Targets and Therapy*. **2013**, 6, 1221-1229.

Nah, J., Pyo, J., Jung, S., Yoo, S., Kam , T., Chang, J., *et al.* BECN1/Beclin1 is recruited into lipid rafts by prion to activates autophagy in response to amyloid β 42. *Autophagy.* **2013**, 9, 1-13.

Narayanan, R.T., Egger, R., Johnson, A.S., Mansvelder, H.D., Sakmann, B., de Kock, C.P.J., and Oberlaender. Beyond columnar organization: cell type- and target layer-specific principles of horizontal axon projection patterns in rat vibrissal cortex. *Cerebral Cortex*. **2015;**1-19.

Neumann, H., Kotter, M.R., and Franklin, R.J.M. Debris clearance by microglia: an essential link between degeneration and regeneration. *Brain*. 132; 288-295; **2009**.

Nishina, K., Jenks, S., & Supattapone, S. Ionic strength and transition metals control PrPSc protease resistance and conversion-inducing activity. *The Journal of Biological Chemistry*. **2004**, 279, 40788-40794.

Nizuma, K., Yoshioka, H., Chen, H., Lim, G.S., Jung, J.E., et al., Mitochondrial and apoptotic neuronal death signaling pathways in cerebral ischemia. *Biochimica et Biophysica Acta*. 1802; 92-99; **2010**.

Nordberg, J., and Arnér, E.S.J. Reactive oxygen species, antioxidants, and the mammalian thioredoxin systems. *Free Radical Biology and Medicine*. 31(11); 1287-1312; **2001**.

Nowak, M., A., Krakauer, D., C., Klug, A., and May, R., M. Protein Infection Dynamics. *Integrative Biology Issues News and Reviews*. **1998**, 1(1), 3-15.

Oberlaender, M., de Kock, C.P.J., Bruno, R.M., Ramirez, A., Meyer, H.S., and Dercksen, V.J. Cell type – specific three-dimensional structure of thalamocortical circuits in a column of rat vibrissal cortex. *Cerebral Cortex.* **2012;** 22; 2375-2391**.**

Öllinger, K. and Brunk, U. T., Cellular injury induced by oxidative stress is mediated though lysosomal damage. *Free Radical Biology and Medicine*. **1995**, 19, 565-574.

Oyadomari, S., and Mori, M. Roles of CHOP/gADD153 in endoplasmic reticulum stress. *Cell Death and Differentiation*. 11; 381-389; **2004**.

Pan, J., Chang, Q., Wang, X., Son, Y. ,Zhang, Z, Chen, G.et al. Reactive oxygen species activated Akt/ASK1/p38 signalling pathway in nickel compound-induced apoptosis in BEAS 2B cells. *Chem. Res. Toxicol*. 23; 568-577; **2010.**

Peferoen, L., Kipp, M., van der Valk, P., van Noort, J. M., & Amor, S. Oligodendrocyte-microglia cross-talk in the central nervous system. *Immunology*. **2013**, 304-313, 141.

Peters, P.J., Mironov Jr., A., Peretz, D., van Donselaar, E., Leclerc, E., Erpel, S., et al. Trafficking of prion proteins through a caveolae-mediated endosomal pathway. *The Journal of Cell Biology*. 162(4); 703-717; **2003**.

Priller, J., Prinz, M., Heikenwalder, M., Zeller, N., Schwarz, P., Heppner, F. L., and Aguzzi, A. Early and rapid engraftment of bone marrow-derived microglia in scrapie. *The Journal or Neuroscience*. 26(45); 11753-11762; **2006**.

Rajendran, L., and Simmons, K. Lipid rafts and membrane dynamics. The Journal of Cell Science. 118; 1099-1102; **2005**.

Redox Chemistry/ Reaction Rates. *Network: Computation in Neural Systems*. 5; 175-189; **1994**.

Ricci, J., Gottlieb, R.A., and Green, D.R. Caspase-mediated loss of mitochondrial function and generation of reactive oxygen species during apoptosis. *The Journal of Cell Biology*. 160; 65-75; **2003**.

Rouvinski, A., Karniely, S., Kounin, M., Moussa, S., Goldberg, M.D., Warburg, G., et al. Line imaging of prions reveals nascent PrPSc in cell-surfsce, raft-assiciated amyloid strings and webs. *The Journal of Cell Biology*. 204(3); 423-441; **2014**.

Safa, J. G., Xiao, X., Kabir, M. E., Chen, S., Lim, C., et al. Structural determinants of phenotypic diversity and replication rate of human prions. *PLOS Pathogens*. **2015**. 11(4). 1-16. 06/02/2015

Sakaguchi, K., Herrera, J. E., Saito, S., Miki, T., Bustin, M., Vassilev, A., et al. DNA damage activates p53 through a phosphorylation-acetylation cascade. *Genes and Developement*. **1998**, 12, 2831-2841.

Sakon, S., Xue, X., Takekawa, M., Sasazuki, T., Okazaki, T., Kojima, Y., et al. NF-kB inhibits TNF-induced accumulation of ROS that mediate prolonged MAPK activation and necrotic cell death. *The EMBO Journal.* 22(15); 38998-3909; **2003**.

Savageau, M.A, Biological Systems Analysis: A Study of Function and Design in Molecular Biology. Reading, MA. 2009.print.

Schilling, M., Besselmann, M., Müller, M., Strecker, J.K., Ringelstein, E.B., amd Kiefer, R. Predominant phagocytic activity of resident microglia over hematogenous macrophages following transient focal cerebral ischemia: an investigation using green flurescent protein transgenic bone marrow chimeric mice. *Experimental Neurology*. 196; 290-297; **2005**.

Shi, Q., Song, Q., Sun, P., Zhang, J., Song, J., Chen, L., *et al*. Infection of prions and treatment of PrP106-126 alter the endogenous status of protein 14-3-3 amd trigger the mitochondrial apoptosis possibly via activating Bax pathway. *Mol Neurobiol*. **2014**, 49, 840-851.

Simon, D., Herva, M.E., Benitez, M.J., Garrido, J.J., Rojo, A.I., Cuadrado, A., et al. Dysfunction of PI3K-Akt-GSK-3 pathway is a common feature in *cell culture* and *in vivo*

Sinclair, L., Lewis, V., Collins, S.J., & Haigh, C. L. Cytosolic caspase mediate mislocalised SOD2 in an *in virto* model of chronic prion infection. *Disease Models and Mechanisms*. **2013**, 6, 952-963.

Sinclair, L., Lewis, V., Collins, S.J., & Haigh, C. L. Cytosolic caspase mediate mislocalised SOD2 in an *in virto* model of chronic prion infection. *Disease Models and Mechanisms*. **2013**, 6, 952-963.

Singh, N., Das, D., Singh, A., and Mohan, M., L. Prion protein and metal interactionL physiological and pathological implications. Current Issues in Molecular Biology. **2012**, 12, 99-108.

Singh, N., Das, D., Singh, A., and Mohan, M., L. Prion protein and metal interactionL physiological and pathological implications. Current Issues in Molecular Biology. **2012**, 12, 99-108.

Sorra, K.E. and Harris, K.M. Occurrence and three-dimensional structure of multiple synapse between individual radiatum axons and their target pyramidal cells in hippocampal area CA1. *The Journal of Neuroscience*. **1993;**13(9):3736-3748.

Soto, C., & Satani, N. The intricate mechanisms of neurodegeneration in prion diseases. *Trends Mol Med.* **2012,** 1-22.

Soto, C., & Satani, N. The intricate mechanisms of neurodegeneration in prion diseases. *Trends Mol Med.* **2012,** 1-22.

Spruston, N. Pyramidal neurons: dendritic structure and synaptic integration. *Nature Reviews Neuronscience*. 9; 206-221. **2008**.

Taylor, D.R., and Hooper, N.M. The prion protein and lipid rafts. Molecular Membrane Biology. 23(1); 89-99; **2006**.

Toddd, D.J., Lee, A., and Glimcher, L.H. The endoplasmic reticulum stress response in immunity and autoimmunity. *Nature Reviews Immunology*. 8; 663-674; **2008**.

Tramo, M.J., Loftus, W.C., Mott, L.A., Green, R.L., Thomas, C.E., and Gazzaniga, M. Surface area of human cerebral cortex and its gross morphological subdivisions: in vivo measurements in monozygotic twins suggest differential hemisphere effects of genetic factors. *Journal of Cognitive Neuroscience.* 7(2); 292-301; **1995**.

Uranga, R.M., Katz, S., and Salvador, G.A. Enhanced phosphatidylinositol 3-kinase (PI3K)/Akt signaling has pleiotropic targerts in hippocampal neurons exposed to iron-induced oxidative stress. *The Journal of Biological Chemistry*. 288(27); 19773-19784; **2013**.

Urayama, A., Morales, R., Niehoff, M.L., Banks, W.A., and Soto, C. Initial fate of prions upon peripheral infection: half-life, distribution, clearance, and tissue uptake. *The FASEB Journal*. 25(8); 2792-2803; **2011**.

Urrutia, O. J., Mena, N.P., & Núñez, M. T. The interplay between iron accumulation, and inflammation during the execution step of neurodegenerative disorders. *Frontiers In Pharmacology.* **2014***,* 5, 1-12.

Urso, E., Manno, D., Serra, A., Buccolieri, A., Rizzello, A., Danieli, A., *et al*. Role of cellular prion protein in neuron adaptation strategy to copper deficiency. *Cell Mol Neurobiol*. **2012**, 32, 989-1001.

Urso, E., Manno, D., Serra, A., Buccolieri, A., Rizzello, A., Danieli, A., *et al*. Role of cellular prion protein in neuron adaptation strategy to copper deficiency. *Cell Mol Neurobiol*. **2012**, 32, 989-1001.

Uttara, B., Singh, A. V., Zamboni, P., & Mahajan, R. T. Oxidative stress and neurodegenerative disease: a review of upstream and downstream antioxidant therapeutic options. *Current Neuropharmacology*. **2009***,* 7, 65-74.

van Aerde, K.I. and Feldmeyer, D. Morphological and physiological characterization of pyramidal neuron subtypes in rat medial prefrontal cortex. *Cerebral Cortex*. **2013**.

Watt, N. T., Griffiths, H. H., & Hooper, N. M. Neuronal zinc regulation and the prion protein. *Prion*. **2013**, 7, 203-208.

Witting, A., Müller, P., Herrmann, A., Kettenmann, H., and Nolte, C. Phagocytic clearance of apoptotic neurons by microglia/brain macrophages in vitro: involvement of lectin-, integrin-, and phospahatidylserine-medited recognition. *Journal of Neurochemistry*. 75; 1060-1070; **2000**.

Wojtera, M., Sobów, T., Kłoszewska, I., Liberski, P. P., Brown, D. R., & Sikorska. B. Expression of immunohistochemical markers on microglia in Creutzfeldt-Jakob disease and Alzheimer's disease: morphometric study and review of literature. *Folia Neuropathologica.* **2012***,* 50, 74-84.

Wong, B. X., & Duce, J. A. The iron regulatory capability of the major protein participants in prevalent neurodegenerative disorders. *Frontiers in Pharmacology.* **2014***,* 5, 1-10.

Xu, C., Bailly-Maitre, B., and Reed, J. C. Endoplasmic reticulum stress: cell life and death decisions. *The Journal of Clinical Investigation*. **2005**, 115, 2656-2664.

Xu, Y., Wang, S., Xie, W., Guo, Y., Zhang, J., Shi, Q., et al. Activation of the macroautophagic system in scrapie-infected experimental animals and human genetic prion diseases. *Autophagy*. **2012;** 8(11); 1604-1620.

Younan, N. D., Nadal, R. C., Davies, P., Brown, D. R., & Viles, J. H. Methionine oxidation perturbs the structural core of the prion protein suggests a generic misfolding pathway. *The Journal of Biological Chemistry*. **2012**, 287, 28263-28275.

Zhao, X., Wang, H., Sun, G., Zhang, J., Edwards, N.J. and Aronowski, J. Neuronal interleukin-4 as a modulator of microglial pathways and ischemic brain damage. The Journal of Neuroscience. 35(32); 11281-11291; 2015.

Zhou, L. and Zhu, D. Neuronal nitric oxide synthase: Structure, subcellular localization, regulation, and clinical implications. *Nitric Oxide*. **2009**, 20, 223-230.

# Appendix

Images of CellDesigner Model  Appearing in the following order:

1. Localization and Trafficking
2. Mitochondria
3. Neuronal Signaling
4. Mircrolgia

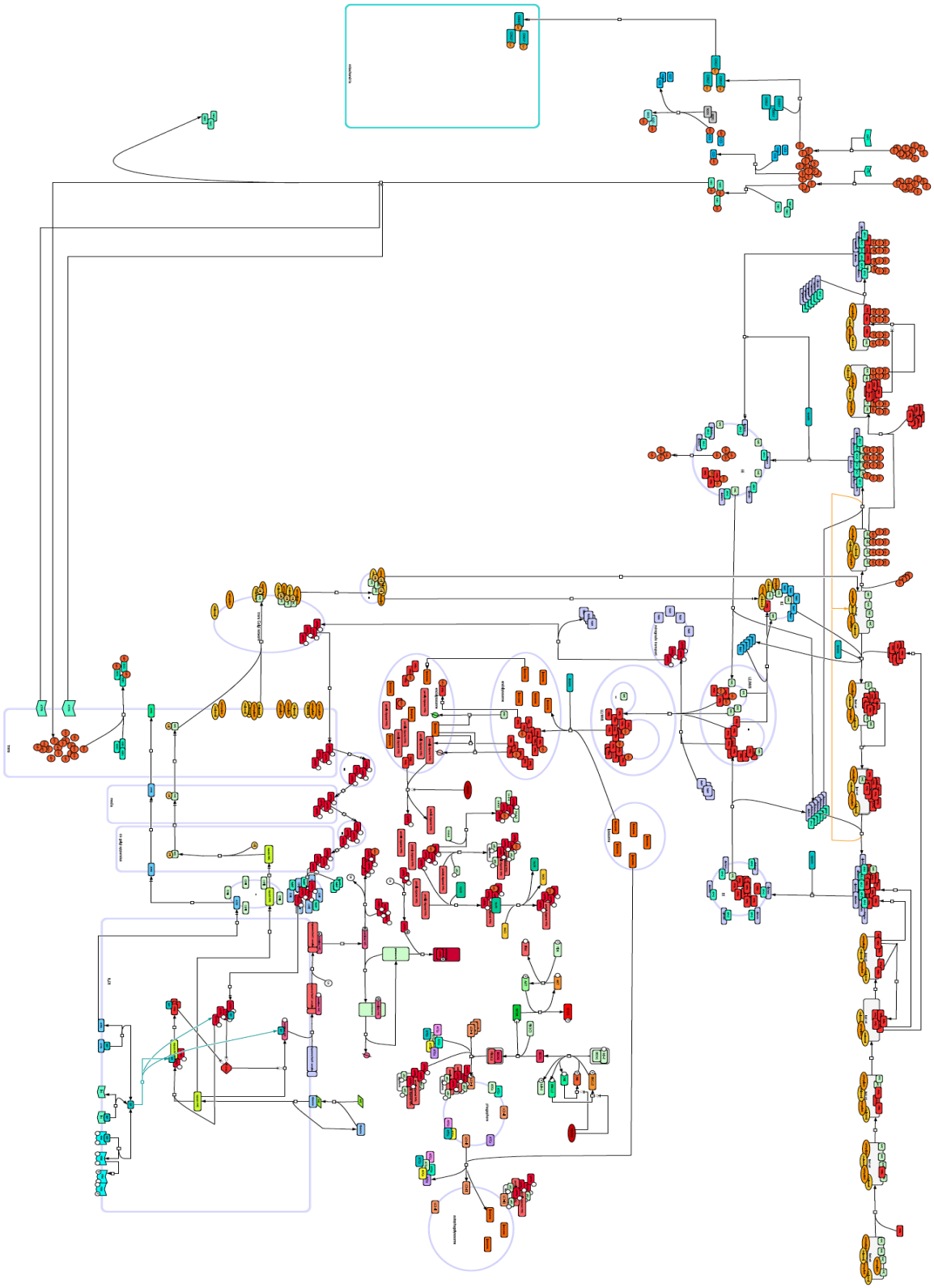

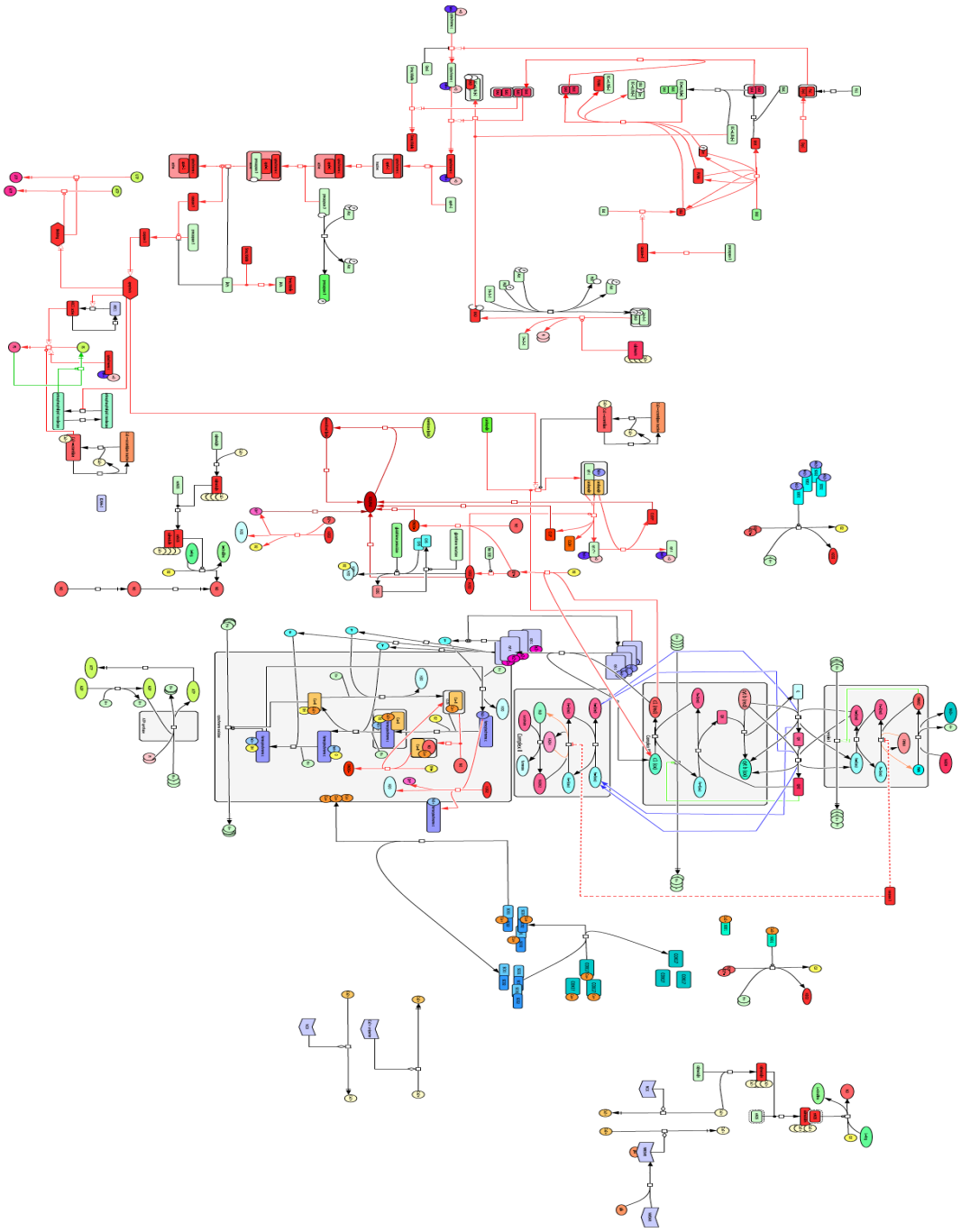

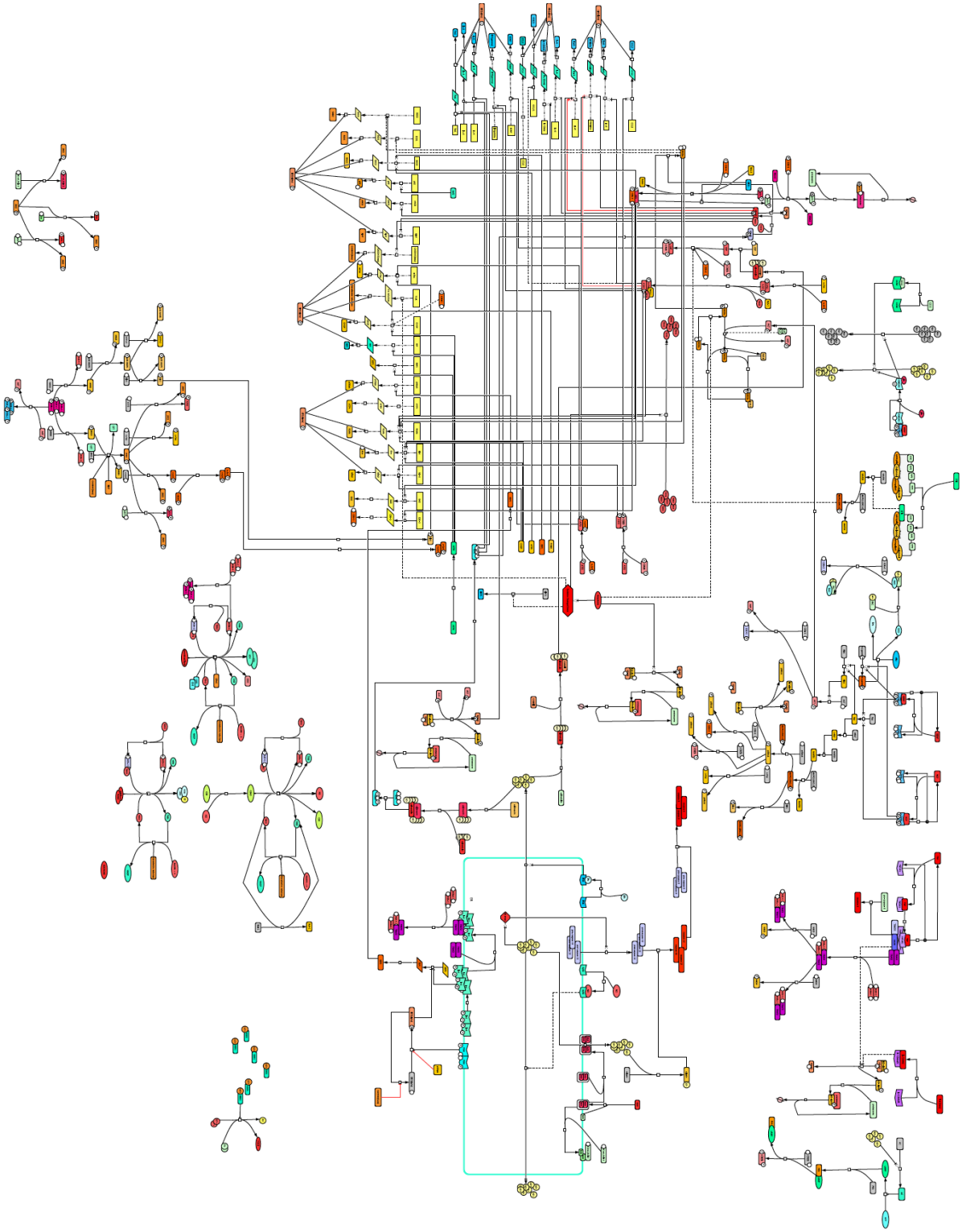

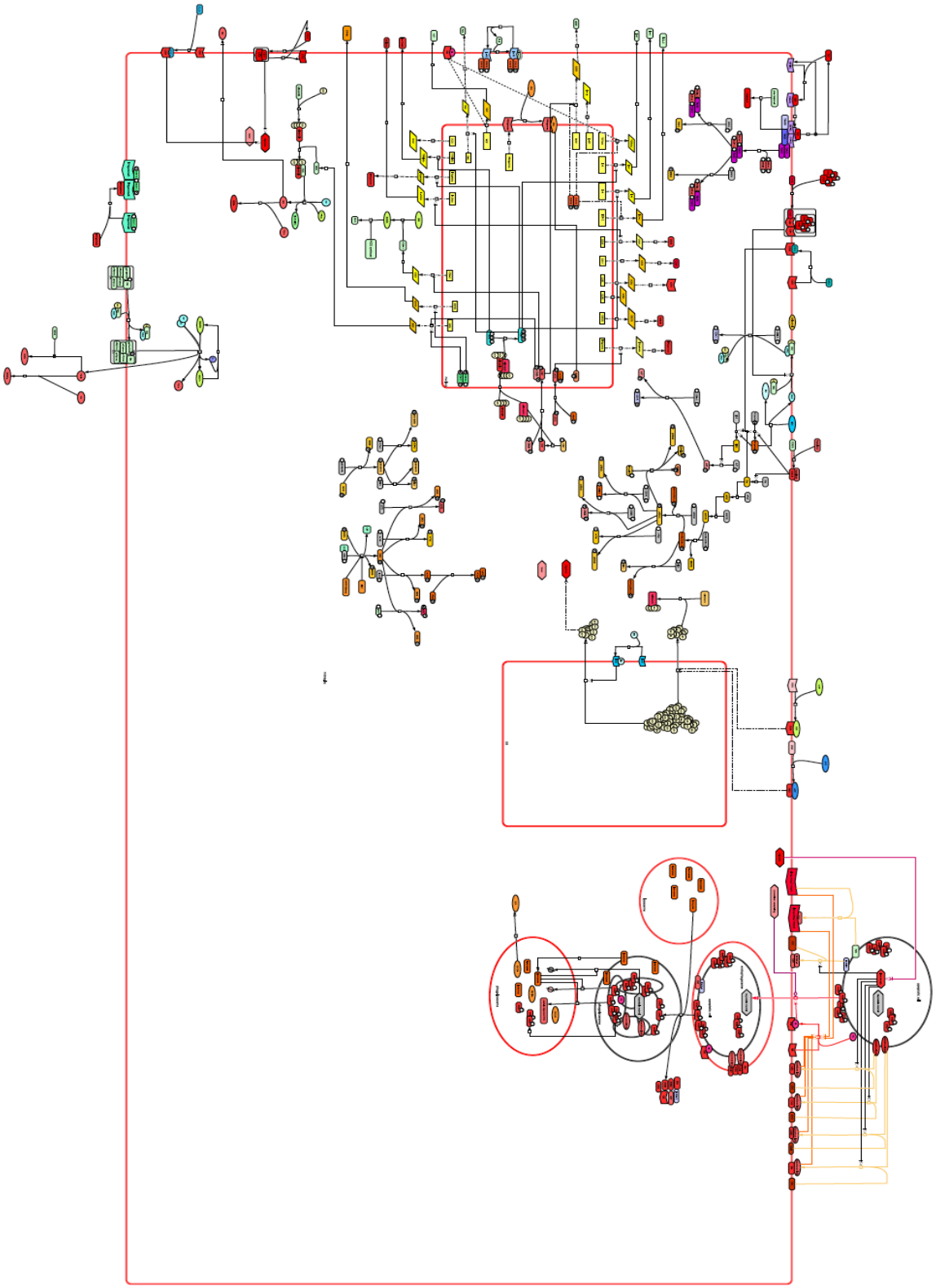

Code is included in the supplementary material.